



Controls on the hydrogen isotope composition of tetraether lipids in an autotrophic ammonia-oxidizing marine archaeon

W.D. Leavitt^{a,b,*}, S.H. Kopf^{c,1}, Y. Weber^{d,2}, B. Chiu^{a,3}, J.M. McFarlin^{c,e}, F.J. Elling^{d,f}, S. Hoefft-McCann^{d,4}, A. Pearson^{d,1}

^a Department of Earth Sciences, Dartmouth College, United States

^b Department of Chemistry, Dartmouth College, United States

^c Department of Geological Sciences, University of Colorado Boulder, Boulder, CO 80309, United States

^d Department of Earth & Planetary Sciences, Harvard University, United States

^e Department of Geology & Geophysics, University of Wyoming, United States

^f Leibniz-Laboratory for Radiometric Dating and Isotope Research, Kiel University, Germany

ARTICLE INFO

Associate editor: Shucheng Xie

Keywords:

Archaeal lipids

GDGTs

Biphytanes

Biomarkers

ABSTRACT

The stable hydrogen isotope composition of persistent biomolecules is used as a palaeohydrological proxy. While much previous work has focused on plant leaf wax-derived *n*-alkanes, the potential of prokaryotic lipid biomarkers as carriers of H isotope signatures remains underexplored, particularly in the Archaea. Here we investigated H isotope distributions in the membrane lipids of the ammonia-oxidizing chemoautotroph *Nitrosopumilus maritimus* strain SCM1. Hydrogen isotope ratios were measured on the cleaved biphytane chains of tetraether membrane lipids extracted from steady-state continuous cultures cultivated at slow, medium, and fast growth rates. In contrast to recent work on bacterial fatty acids, where the direction and magnitude of isotopic fractionation varies widely (*ca.* 600‰ range) as a function of central C and energy metabolism, archaeal biphytane data in the present work are relatively invariant. The weighted average ²H/¹H fractionation values relative to growth water (²ε_{L/W}) ranged from −272 to −260‰, despite a three-fold difference in doubling times (30.8–92.5 hr), yielding an average growth-rate effect <0.2‰ hr^{−1}. These ²ε_{L/W} values are more negative than most heterotrophic microbial lipid H isotope measurements in the literature, and are on par with those from other autotrophic archaea, as well as with phytol from photoautotrophic algae. *N. maritimus* values of ²ε_{L/W} also varied systematically with the number of internal rings (cyclopentyl + cyclohexyl), increasing for each additional ring by 6.4 ± 2.7‰. Using an isotope flux-balance model in tandem with a comprehensive analysis of the sources of H in archaeal lipid biosynthesis, we use this observation to estimate the kinetic isotope effects (KIEs) of H incorporation from water; from reducing cofactors such as flavins and NADPH, and for the transhydrogenation reaction(s) that convert the electron-donor derived NADH into these cofactors. Consistent with prior studies on bacteria and plants, our results indicate the KIEs of reducing cofactors in archaea are highly fractionating, while those involving exchange of water protons are less so. When combined with the observation of minimal growth-rate sensitivity, our results suggest biphytanes of autotrophic 3HP/4HB utilizing Nitrososphaerota (a.k.a. Thaumarchaeota) may be offset from their growth waters by a nearly constant ²ε_{L/W} value. Together with the ring effect, this implies that all biphytanes originating from a common source should have a predictable ordering of their isotope ratios with respect to biphytane ring number, allowing precise reconstruction of the original δ²H value of the environmental water. Collectively, these patterns indicate archaeal biphytanes have potential as paleo-hydrological proxies, either as a complement or an alternative to leaf wax *n*-alkanes.

* Corresponding author at: Department of Earth Sciences, Dartmouth College, United States.

E-mail address: william.d.leavitt@dartmouth.edu (W.D. Leavitt).

¹ Contributed equally.

² Current address: Beam Therapeutics, United States.

³ Current address: c16 biosciences, United States.

⁴ Current address: Wellesley College, United States.

1. Introduction

The relative abundances of protium (^1H) and deuterium (^2H) in water track a wide variety of physical, hydrological, and climate parameters (Gat, 1996; Hayes, 2001; Robert, 2001). Certain biomolecules incorporate these isotopes at predictable ratios ($\delta^2\text{H}$ values) relative to their source water, preserving a record of conditions at the time of synthesis. Indeed some lipid hydrogen isotope compositions can survive in the sedimentary record for millions of years, encoding past changes in Earth system processes, from tectonics to hydroclimate to local ecology (Dawson et al., 2004; Schimmelmann et al., 2006; Sessions, 2016; Sessions et al., 2004). The H isotopic ratios of biomolecules utilized for reconstructing past environments and ecologies have been studied broadly in photoautotrophic organisms, as well as in a variety of chemoautotrophic and heterotrophic bacteria (e.g., Dawson et al., 2015; Maloney et al., 2016; Osburn et al., 2016; Sachs et al., 2016, 2017; Sachs and Kawka, 2015; Sessions et al., 1999; Wolfshorndl et al., 2019; Zhang et al., 2009). To date, however, there are few reports of H isotope values for the archaea (Dirghangi and Pagani, 2013; Kaneko et al., 2011; Lengger et al., 2021; Wu et al., 2020). In part this taxonomic bias originates from the long history of experimental and field study on leaf plant waxes and marine phytoplankton (Estep and Hoering, 1980; Sachs, 2014; Sachse et al., 2012; Sessions et al., 1999). This is especially due to the analytical challenges in the H isotope analysis of archaeal ether lipids (Lengger et al., 2021), as well as the still emerging picture of how archaeal biomarkers are biosynthesized (Jain et al., 2014; Lloyd et al., 2022; Oger and Cario, 2013; Pearson, 2019; Zeng et al., 2019, 2022). Ultimately this leaves our understanding of how archaeal lipids reflect environmental and growth water $\delta^2\text{H}$ values incomplete. Unlocking the historical archive of archaeal lipid H isotopes requires examining the biochemical controls on their lipid-water isotope fractionation ($^2\varepsilon_{\text{L/W}}$).

The expression of $^2\varepsilon_{\text{L/W}}$ in geostable water reflects not only incorporation of environmental water, but also the kinetic isotope effects (KIEs) of enzymes involved in energy conservation, central metabolism, and the pathway(s) of lipid biosynthesis. Trends in the $^2\varepsilon_{\text{L/W}}$ between growth water and long-chain *n*-alkanes (plant waxes) from plants and eukaryotic algae, capture changes in hydroclimate (Hou et al., 2008; Kahmen et al., 2011; McInerney et al., 2011; Sachse et al., 2012, 2010; Smith and Freeman, 2006), although up to a quarter of the observed variance could also be due to genetic factors (Bender and Suess, 2016). Experimental calibration of lipid $^2\varepsilon_{\text{L/W}}$ from eukaryotic microalgae has focused on constraining the response to physical parameters such as temperature, salinity, irradiance, and growth rate (Maloney et al., 2016; Sachs, 2014; Sachs et al., 2016, 2017; Sachs and Kawka, 2015; van der Meer et al., 2015; Wolfshorndl et al., 2019).

In contrast to eukaryotic examples, bacterial lipids show considerably more range in $^2\varepsilon_{\text{L/W}}$ values. Multiple taxa have been studied with respect to their $^2\varepsilon_{\text{L/W}}$ offsets from growth water, as well as for differences between metabolism-specific processes, and the use of different substrates (Campbell et al., 2017, 2009; Dawson et al., 2015; Heinzlmann et al., 2018, 2015; Leavitt et al., 2016a,b, 2017; Osburn et al., 2016; Sessions et al., 2002, 1999; Valentine et al., 2004; Wijker et al., 2019; Zhang et al., 2009). Such work shows that $^2\varepsilon_{\text{L/W}}$ can be exceptionally large in bacteria, varying by tens of percent in both the positive and negative directions. Broad patterns in $^2\varepsilon_{\text{L/W}}$ values can distinguish bacterial chemoautotrophs (–400 to –200‰), photoauto(hydro)trophs (–250 to –150‰), and (an)anaerobic heterotrophs (–150 to +300‰) (Sessions et al., 2002; Valentine et al., 2004; Kreuzer-Martin et al., 2006; Campbell et al., 2009, 2017; Zhang et al., 2009; Dawson et al., 2015; Heinzlmann et al., 2015; Leavitt et al., 2016a,b, 2017; Osburn et al., 2016; Wijker et al., 2019).

Patterns of $^2\varepsilon_{\text{L/W}}$ may also vary for different lipid biosynthetic classes. While many hydroclimate applications focus primarily on acetogenic (*n*-alkyl) lipids (e.g., *n*-alkanes, fatty acids, alkenones), there also is promise in the study of isoprenoid structures. The generally more negative $^2\varepsilon_{\text{L/W}}$ values reported in isoprenoid lipids relative to acetogenic

lipids was initially identified in higher plants and algae (Estep and Hoering, 1980; Sessions et al., 1999). Isoprenoid lipids – specifically phytol chains of chlorophyll – become more ^2H -depleted with increasing degree of saturation, where the stepwise hydrogenation of geranylgeraniol (from cucumber), with a starting composition of –281‰, ultimately yields isotopically lighter phytol at –345‰ (Chikaraishi et al., 2009). The implication is that enzymatic saturation of long-chain polyisoprenes generates consistently lower $\delta^2\text{H}$ -lipid values, regardless of biosynthetic pathway or organism.

Archaea generate some of the most diagenetically robust and structurally diagnostic isoprenoid lipids yet have been little studied. Natural abundance lipid $\delta^2\text{H}$ studies have been conducted with a mesophilic halophile (Dirghangi and Pagani, 2013), a couple of thermoacidophiles, as well as a handful of natural sediment samples (Kaneko et al., 2011; Lengger et al., 2021). Additionally, one study has worked on an axenic culture of methanogen on different substrates and water ^2H (spike) compositions (Wu et al., 2020), while others have focused on co-cultures of anaerobic methane oxidizing archaea (Kellermann et al., 2016; Wegener et al., 2016). The archaeal biomarkers most critical to paleo-environmental reconstructions are the glycerol dibiphytanyl glycerol tetraethers (iGDGTs) (Pearson and Ingalls, 2013; Schouten et al., 2013, 2002), compounds that are found as a series of structural homologs containing from zero to eight cyclopentane rings (most commonly ≤ 6 ; iGDGT-0, –1, ... –6) (De Rosa and Gambacorta, 1988); or in the case of crenarchaeol – a lipid unique to the Nitrososphaerota (syn. Thaumarchaeota) – one cyclohexane and four cyclopentane rings (Damsté et al., 2002). The primary application of iGDGT biomarkers to date has been marine paleothermometry (Schouten et al., 2002), which requires calibration of iGDGT ring distributions to growth temperature and other environmental forcing, both in the laboratory and in modern core-top samples (e.g., Cobban et al., 2020; Dunkley Jones et al., 2020; Elling et al., 2017; Hurley et al., 2016; Kim et al., 2008, 2010; Tierney and Tingley, 2014, 2015; Zhou et al., 2020). The ring distributions of thermoacidophiles provide important context to this work by investigating the interaction between temperature changes and other growth determinants such as pH, energy availability, and redox status (Boyd et al., 2011, 2013; Feyhl-Buska et al., 2016; Quehenberger et al., 2020; Tourte et al., 2022; Yang et al., 2023; Zhou et al., 2020, 2020). Similarly detailed work is needed to understand the $^2\varepsilon_{\text{L/W}}$ isotope compositions of iGDGTs such that we may evaluate their potential as hydrologic cycle proxies.

In this study we determined the H isotope fractionation between iGDGTs and growth water for the ammonia-oxidizing archaeal (AOA) chemoautotroph *Nitrosopumilus maritimus* SCM1. Strain SCM1 was cultivated continuously under chemically static (chemostat) conditions at a range of cellular doubling times. The growth and metabolic rates were controlled by increasing or decreasing the energy flux via different medium supply rates, where the primary electron donor (either ammonium or sucrose) was limiting. For prior examples of this approach with archaea, see studies by: (Hurley et al., 2016; Quehenberger et al., 2020; Zhou et al., 2020). For all trials, we quantified the magnitude of $^2\varepsilon_{\text{L/W}}$ for the full set of biphytane (BP) hydrocarbons liberated by ether cleavage from acid extractable total iGDGTs. We present values from BP-0, BP-1, BP-2, and BP-3. The results indicate that $^2\varepsilon_{\text{L/W}}$ for *N. maritimus* remains nearly constant between fast, medium, and slow growth rates, suggesting that the ubiquitous iGDGTs of mesophilic autotrophs have potential as paleohydrological proxies. The hydrogen isotope ratios of mesophilic archaeal iGDGTs and their derivative BPs may be reliably and consistently offset from local growth waters.

2. Methods

2.1. Culture conditions

Continuous (chemostat) cultures of *N. maritimus* SCM1 were grown on modified Synthetic Crenarchaeota Medium with 1 mM NH_4Cl as

previously described (Hurley et al., 2016; Martens-Habben et al., 2009), but with the following modifications: 300 μM α -ketoglutaric acid was added as a H_2O_2 scavenger (Bayer et al., 2019; Kim et al., 2016), and a balance-controller loop was used to maintain a constant dilution rate (my-Control™, Applikon, Delft, the Netherlands). In the 1.6 L reactor temperature was held constant at 28 °C, and the pH of the initial medium was adjusted to 7.8, which yielded *in situ* pH of 7.52–7.56 over the course of the experiments at steady state. Nitrite concentrations and pH values for *N. maritimus* remained stable within analytical precision (nitrite \pm 0.03 mM; pH \pm 0.01). The *N. maritimus* experiments were run in a single bioreactor and maintained steady state conditions throughout the sampling intervals. The dilution rate was set to yield cell doubling times (T_D) of 30.8, 46.2, and 92.5 h. Upon reaching steady state, the outflow of each bioreactor was collected continuously into a chilled vessel (0–4 °C) for between 1 and 4 days, representing a complete turnover at the specified rate. *N. maritimus* cells were isolated by filtration onto combusted 0.3 μm GF-75 glass fiber filters (Sterlitech, Kent, WA, USA). Filters were stored at –80 or –20 °C until processing for lipid analysis.

2.2. Lipid extraction and biphytane preparation

Core iGDGTs were extracted from freeze-dried pellets and filters by acid hydrolysis followed by ultrasonic solvent extraction as described previously (Zhou et al., 2020). Briefly, samples were incubated in 3 N methanolic HCl (33% water content) for 90 min at 65 °C. Methyl *tert*-butyl ether (MTBE) was added at a ratio of 3:2 (acid:MTBE, v:v), and samples were sonicated for 5 min (Qsonica Q500, Newtown, CT, USA). After sonication, *n*-hexane was added at a ratio of 1:1 (MTBE:hexane, v:v), vortexed, and centrifuged (3 min, 15,000g). The organic upper layer was collected, dried under N_2 , and separated into two fractions over activated Al_2O_3 by elution with dichloromethane (DCM; non-polar lipids), and DCM:methanol (1:1, v:v; iGDGTs). Ether bonds were cleaved in 57% HI (4 hr at 120 °C), and the resulting alkyl iodides were reduced to alkanes (BPs) with H_2 in the presence of $\text{Pt}^{(\text{IV})}\text{O}_2$, a reduction method that does not exchange already-saturated H-C bonds, following the method of (Kaneko et al., 2011). Before analysis, BPs were purified over activated Al_2O_3 by elution with *n*-hexane. Samples of *N. maritimus* were collected in large volumes and reflect single extracts.

2.3. Hydrogen isotope analyses and data reduction

Biphytane $^2\text{H}/^1\text{H}$ ratios were analyzed by gas chromatography pyrolysis isotope ratio mass spectrometry (GC-P-IRMS) on a GC IsoLink II IRMS System (Thermo Scientific), consisting of a Trace 1310 GC fitted with a programmable temperature vaporization (PTV) injector and either a 30 m ZB5HT column (i.d. = 0.25 mm, 0.25 μm , Phenomenex, Torrance, CA, USA) or a 60 m DB1 column (i.d. = 0.25 mm, 0.25 μm , Agilent, Santa Clara, CA, USA), ConFlo IV interface, and 253 Plus mass spectrometer (Thermo Scientific). Sample runs using the ZB5HT column used a fast ramp of the PTV to 400 °C for sample transfer to the GC column and initial hold of the column at 60 °C for 2 min, the GC oven was ramped to 350 °C over the course of 14.5 min at a rate of 20 °C min^{-1} , followed by an isothermal hold at 350 °C for 7 min during which all biphytanes eluted (see Fig. S1). Sample runs using the DB1 column used a fast ramp of the PTV to 330 °C for sample transfer to the GC column and initial hold of the column at 60 °C for 2 min, the GC oven was ramped to 220 °C over the course of 7 min at a rate of 22 °C min^{-1} , then to 330 °C over the course of 14 min at a rate of 8 °C min^{-1} , followed by an isothermal hold at 330 °C for 20 min during which all biphytanes eluted.

All $^2\text{H}/^1\text{H}$ ratios are reported in delta notation ($\delta^2\text{H}$) in permil (‰) units relative to the international seawater standard on the VSMOW-SLAP (Vienna Standard Mean Ocean Water, Standard Light Antarctic Precipitation) scale. All $^2\text{H}/^1\text{H}$ fractionation factors are reported in epsilon notation (ϵ^2) in permil (‰). All peak amplitudes are reported in

volts (V) and refer to the amplitude of the m/z 2 measurement which has an operational amplifier with a $10^9 \Omega$ resistor and thus reflects nA currents. Values of $\delta^2\text{H}$ were first determined relative to H_2 reference gas ($\delta^2\text{H}_{\text{raw}}$), and then calibrated externally using a standard *n*-alkane mixture (A6, containing C_{15} through C_{30} *n*-alkanes spanning from –9 to –263‰ vs. VSMOW; A. Schimmelmann, Indiana University). The A6 standard was combined with a C_{36} *n*-alkane (nC_{36} , –259.2‰ vs. VSMOW; A. Schimmelmann, Indiana University) and measured at regular intervals at different concentrations. The BP hydrogen isotope calibration was performed in R based on 2195 compound-specific measurements from the A6 standard with peak amplitudes from 0.80 to 36 V (m/z 2) using the packages *isoreader* (v 1.3.0, (Kopf et al., 2021)) and *isoprocessor* (v 0.6.11) available at github.com/isoverse. To correct for offset, scale compression and peak-size effects (Fig. S2), the following multivariate linear regression was inverted and applied to all standards and samples to determine $\delta^2\text{H}_{\text{cal}}$:

$$\delta^2\text{H}_{\text{raw}} = \beta_0 + \beta_1 \cdot \delta^2\text{H}_{\text{cal}} + \beta_2 \cdot A + \beta_3 \cdot \delta^2\text{H}_{\text{cal}} \cdot \sqrt{A} \quad (1)$$

where A signifies peak amplitude (m/z 2), and $\delta^2\text{H}_{\text{cal}}$ is the actual H-isotope composition of the analytes (known values for standard compounds; calibrated values for target compounds after inversion). The overall RMSE of calibration was 4.9‰ and residuals showed a random distribution (Fig. S2, Panel 4), whereas other simpler regression models had substantially larger errors and showed systematic trends in their residuals (for a comparison of several different regression models see Fig. S2B). To assess the uncertainty introduced by sample matrix and low signal-to-noise ratios, each biphytane peak was integrated multiple times in the Isodat software (v 3.0, Thermo Scientific), with manual background correction set before and after the eluting analyte peak. This analysis suggested integration errors to be negligible. Finally, to accurately assess peak-size dependent analytical uncertainty, the nC_{36} standard was analyzed throughout in combination with the A6 standard because of its similar retention time to the biphytanes (elutes between BP-0 and BP-1). It was purposefully excluded from the calibration (Eq. (1)) and was instead used to estimate the analytical error of the biphytane H isotope measurements after calibration using a local polynomial regression fit across all 73n-C₃₆ measurements spanning peak amplitudes from 0.06 to 27 V (m/z 2). This provided conservative peak-size adjusted error estimates of the calibrated measurements (σ_{cal}) with steep increases in the observed error at low peak amplitudes stepping from 3.9‰ at analyte peak amplitudes of 5 V to 14‰ at 2 V and 34‰ at 1 V (Fig. S3).

Calibrated $\delta^2\text{H}$ values for the biphytanes were corrected for the H added during hydrogenation of alkyl iodides. Assuming a similar isotope effect associated with the PtO_2 -catalyzed reaction of H_2 and alkyl iodides as previously reported ($\epsilon^2_{\text{hydrog}} = -721 \pm 177\text{‰}$; (Kaneko et al., 2011)), and the measured $\delta^2\text{H}$ value of the H_2 tank ($\delta^2\text{H}_{\text{H}_2} = -64 \pm 2\text{‰}$; courtesy of Andrew Masterson, Northwestern University, IL, USA), the final corrected $\delta^2\text{H}$ values were calculated using the following equation:

$$\delta^2\text{H}_{\text{cor}} = \left(1 + \frac{2}{n_H}\right) \cdot \delta^2\text{H}_{\text{cal}} - \frac{2}{n_H} \cdot ((\epsilon^2_{\text{hydrog}} + 1) \cdot (\delta^2\text{H}_{\text{H}_2} + 1) - 1) \quad (2)$$

where n_H is the number of original H atoms in each alkyl chain. The total analytical uncertainty of the corrected $\delta^2\text{H}$ values was calculated using standard error propagation (Eq. (3)) of the peak-size adjusted error estimates and hydrogenation correction assuming all errors to be uncorrelated. The hydrogenation correction ranged from 10.3 to 12.7‰ and increased analytical uncertainty by up to 1.9‰.

$$\sigma_{\text{cor}} = \sqrt{\left(\frac{\partial(\delta^2\text{H}_{\text{cor}})}{\partial(\delta^2\text{H}_{\text{cal}})} \cdot \sigma_{\text{cal}}\right)^2 + \left(\frac{\partial(\delta^2\text{H}_{\text{cor}})}{\partial(\delta^2\text{H}_{\text{H}_2})} \cdot \sigma_{\text{H}_2}\right)^2 + \left(\frac{\partial(\delta^2\text{H}_{\text{cor}})}{\partial(\epsilon^2_{\text{hydrog}})} \cdot \sigma_{\text{hydrog}}\right)^2} \quad (3)$$

Hydrogen isotope analysis of growth medium water ($\delta^2\text{H}_{\text{water}}$) was conducted with filter-sterilized media samples collected at the time of

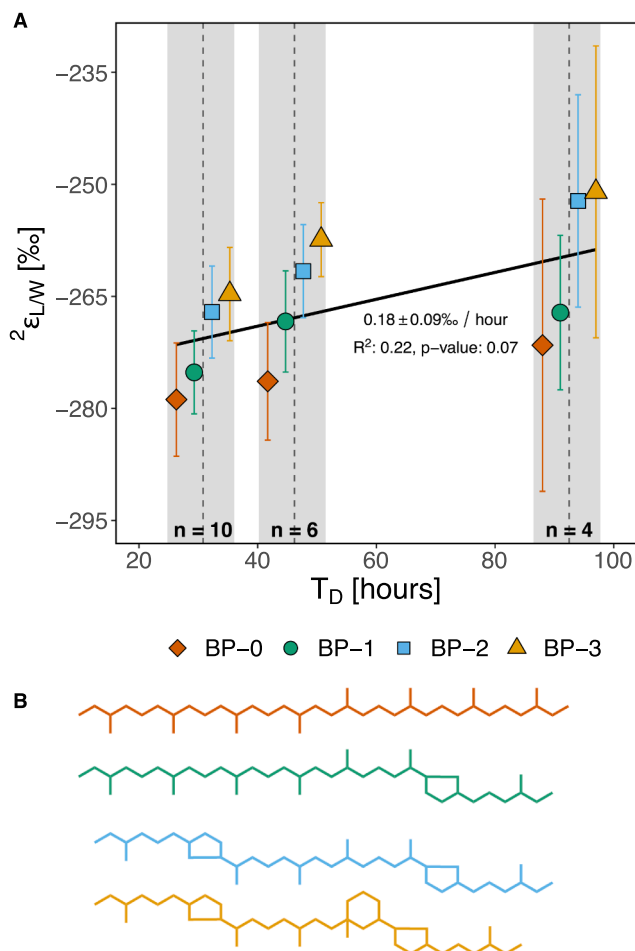


Fig. 1. (A) The hydrogen isotope fractionation ($^2\epsilon_{L/W}$) between growth medium water and biphytanes (BPs) in response to doubling time (T_D) for *N. maritimus* cultivated at 28 °C and pH 7.5–7.6. Black line shows the slope and standard error (‰/hour) for the abundance-weighted linear regression of all biphytane $^2\epsilon_{L/W}$ values vs. T_D (the 95% confidence interval ranges from -0.02 to 0.38 ‰/hour) (B) Structures of the BPs (color-coded to match data shown in A).

4. Isotope flux-balance model

To generalize these findings and pave the way for future work with other archaea, we constructed an isotope flux-balance model (Fig. 2A) to explain both the magnitude of and patterns within the observed $^2\epsilon_{L/W}$ values for *N. maritimus* (Fig. 1). This analysis provides insight into the biochemical origins of archaeal $^2\epsilon_{L/W}$ patterns and highlights their potential for proxy applications.

N. maritimus SCM1 grows autotrophically by the 3-hydroxypropionate/4-hydroxybutyrate (3HP/4HB) cycle, and utilizes NH_4^+ as an electron donor and O_2 as a terminal electron acceptor (Könneke et al., 2014). It was chosen to explore potential impacts of growth rate variability on $^2\epsilon_{L/W}$ patterns expressed by 3HP/4HB utilizing archaea, given the goal of developing an environmental proxy based on BPs of the globally ubiquitous, ammonia oxidizing archaea. Therefore, some sections of our isotope model and the ensuing discussion may not be applicable to all archaea; below we aim to distinguish between universal vs. metabolism-specific information.

4.1. Sources of hydrogen in archaeal lipid synthesis

In chemo(litho)autotrophic archaea, the hydrogen in lipid biosynthesis derives directly from intracellular water, either directly from

proton incorporation and water exchange reactions or indirectly from metabolic hydride carriers (Figs. 2 and 3; Fig. S4). In heterotrophs there is also the potential for incorporation of carbon-bound hydrogen derived from organic substrate (e.g., glucose or acetate). Given the possible complexity, we examined in detail the origin of H in all biosynthetic steps to biphytanes in *N. maritimus* and calculated stoichiometric scenarios to serve as a framework for interpreting $^2\epsilon_{L/W}$ patterns.

4.1.1. Synthesis of archaeal isoprenoids

In archaea, the synthesis of BP hydrocarbons proceeds as follows. Isopentenyl pyrophosphate (IPP) is synthesized from three units of acetyl CoA (Ac-CoA) using the mevalonate pathway (Fig. 3, steps 1–6; (Chen et al., 1994; Hayakawa et al., 2018; Koga and Morii, 2007). Three units of IPP and one of its isomer dimethylallyl pyrophosphate (DMAPP) together condense to yield geranylgeranyl diphosphate (GGPP, not shown; Chen and Poulter, 1993). The hydrogen in IPP derives both from the original acetate and from HMG-CoA reductase using NADPH as co-factor, while isomerization between IPP and DMAPP (Fig. 3, step 6) also incorporates one H from water in place of one originally contributed by acetate. If the formation of DMAPP is limited to the minimum required to initiate isoprenoid condensation (1:3, DMAPP:IPP), only a single terminal H in the resulting GGPP retains the water signature. Additional water H can be introduced either during IPP/DMAPP interconversion (Fig. 3, step 6), and/or potentially during tautomerization of acetoacetyl-CoA (Fig. 3, step 2), where if IPP-DMAPP isomerase is rapid relative to steps 7 and 8, then more water-derived H may be carried into the isoprenoid product. Thus, there is a range of stoichiometry possible for the fractional contribution of water-derived H, the consequences of which are elaborated in section 4.1.2. Condensation of two di-*O*-geranylgeranyl glycerol phosphate (DGGGP) units into the membrane-spanning tetraether by the Tes enzyme eliminates two H, which would be of mixed water and acetate origin (Fig. 3, step 8) (Lloyd et al., 2022; Zeng et al., 2022). Ring formation is catalyzed by GrsA and GrsB (Zeng et al., 2019) (Fig. 3, step 9) and does not add any net hydrogen, but likely replaces some acetate-derived H with water-derived H. Saturation (Fig. 3, step 10) is catalyzed by geranylgeranyl reductase (GGR). GGR is an FAD-dependent flavoenzyme that reduces the prenyl double bonds, and is itself reduced by a metabolic reductant (Isobe et al., 2014; Nishimura and Eguchi, 2006; Sasaki et al., 2011). NADPH serves as the biological reducing agent for GGR-bound flavin in plants and cyanobacteria (Addlesee et al., 1996; Keller et al., 1998), in contrast to NADH in *Thermoplasma acidophilum* cell extracts (Nishimura and Eguchi, 2006). In other archaea, neither NADH nor NADPH reduce GGR *in vitro*, whereas reductants such as ferredoxin or F420 have been implicated in *Archaeoglobus fulgidus* (Murakami et al., 2007), *Sulfolobus acidocaldarius* (Sato et al., 2008), and *Methanosarcina acetivorans* (Isobe et al., 2014), though these may work in concert with NAD(P)H. The *in vivo* GGR reductant in *N. maritimus* remains unknown. Nonetheless, the GGR saturation reaction introduces a hydride (H^-) and a proton (H^+) per double bond. Overall, these enzymatic steps lead to the following stoichiometric accounting for archaeal biphytanes.

4.1.2. Stoichiometric accounting: H sources in archaeal biphytanes

Most of the 80 H atoms in the C_{40} alkyl chain of the acyclic biphytane (BP-0) are inherited from methyl-H of Ac-CoA (f_A , fractional contribution from Ac-CoA). Hydrides (H^-) are introduced from NADPH during biosynthesis of the mevalonate precursor to IPP ($f_{LS_{\text{NADPH}}}$), as well as during the final saturation of the alkyl chains by GGR-bound flavin ($f_{GGR_{\text{FAD}}}$); the paired protons (H^+) are obtained from water (f_{LS_w} , f_{GGR_w}) and additional water is introduced during ring synthesis (f_{RS_w}). Finally, if water is assumed to exchange freely with acetoacetyl-CoA during synthesis of IPP and DMAPP and IPP may isomerize, the model contains an exchangeable water fraction (f_x) (Eq. (5a)).

For any archaeon that grows as an autotroph, all three H of the Ac-CoA methyl group also derive originally from water. These H can be conceptualized as (i) direct incorporation of cellular water, or (ii)

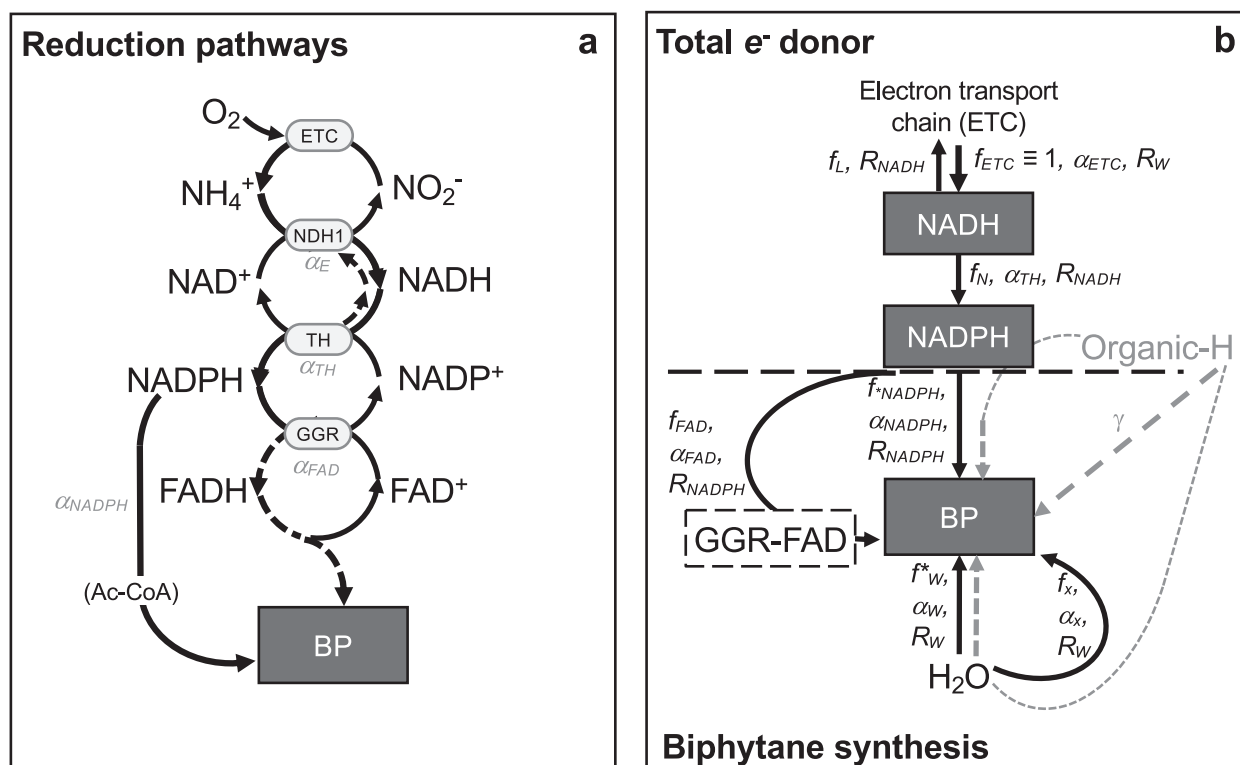


Fig. 2. (A) Sources of biosynthetic H for biphytane (BP) synthesis in *N. maritimus*. Ammonia monooxygenase and the electron transport chain (ETC) donate electrons to reduce respiratory complex 1 (NDH1), from which an unknown transhydrogenase (TH) transfers H to NADPH. This NADPH either is a direct source of anabolic H to BPs (via Ac-CoA and further reactions; see Fig. 3) or the e⁻ are transferred to geranylgeranyl reductase (GGR), which uses a flavin cofactor (GGR-FAD). See main text for further details. (B) The resulting isotope flux balance model with simplified sources of H. The budget of total harvested electron donor sums above the horizontal dashed line, whereas biphytane synthesis sums below the line. Thus, f_N and f_{NADPH} are not equal; f_N is a fraction of total available reducing power, f_{ETC} (with the remainder leaked via the NADH pool, f_L), while f_{NADPH} is a fraction of biphytane stoichiometric flux. Processes that would incorporate H from acetate and organic substrates are shown in grey: thin dashed arrows signify the partitioning of de novo (autotrophic) acetate H into the NADPH and H₂O pools, while the fraction (γ) of acetate methyl groups that is inherited directly from organic substrates is shown with a long-dashed arrow; in *N. maritimus*, γ is always zero. f_i = fractional fluxes; $\alpha_i = {}^2\text{H}/{}^1\text{H}$ kinetic isotope effects; $R_i = {}^2\text{H}/{}^1\text{H}$ isotope ratios; concept according to Wijker et al. (2019). Details about the specific stoichiometry for each BP are shown in Fig. 3 and Tables 2, 3, and S2.

donation from reducing cofactors. The stoichiometric budget for biphytane H sources in *N. maritimus* can therefore be simplified for isotope flux balance analysis: H derived directly from water via acetyl Co-A synthesis (f_{AW}), lipid biosynthesis (f_{LSw}), ring synthesis (f_{RSw}), and GGR reduction (f_{GGRw}) are combined to yield total direct water H (f_{w}); NADPH-derived hydrides (ultimately also from water H but differently fractionated) for the synthesis of acetyl CoA (f_{ANADPH}) and downstream lipid biosynthesis ($f_{LSNADPH}$) are combined to yield total NADPH sources (f_{NADPH}); while the flavin-derived GGR hydride is kept separately as f_{FAD} (Eq. (5b)).

$$BP = f_A + f_{LSw} + f_{RSw} + f_{GGRw} + f_{LSNADPH} + f_{GGRFAD} + f_x \quad (5a)$$

$$BP = (f_{AW} + f_{LSw} + f_{RSw} + f_{GGRw}) + (f_{ANADPH} + f_{LSNADPH}) + f_{GGRFAD} + f_x = f_{w} + f_{NADPH} + f_{FAD} + f_x \quad (5b)$$

The 3HP/4HB cycle generates Ac-CoA with a predicted ratio of 2:1 for water-derived and NADPH-derived H using reasonable biochemical assumptions for the mechanism of each step (Fig. S4). Thus, when there is no direct incorporation of H from organic substrates, the H assigned to Ac-CoA can be apportioned 0.67:0.33 among the water (f_{AW}) and NADPH (f_{ANADPH}) pools (Table S1). Aspects of this accounting model are widely applicable across the archaea, i.e., are not specific to the 3HP/4HB-pathway, and later can be utilized for other autotrophs as well as heterotrophs.

4.1.3. Summary budget and the impact of ring number

The number of rings (r) changes the total number of H in biphytanes

(n) as well as the fractional contribution of each H source (f_i). The denominator (n) reflects that for each additional ring, the molecule has 2 fewer H overall. The stoichiometry of adding a ring is more complicated than eliminating the incorporation of one H⁻ from GGR-FAD and one H⁺ from water. Up to one H per ring is replaced by GrsAB during ring cyclization due to the S-adenosylmethionine radical mechanism (Pearson, 2019) of the recently discovered GrsA/B enzyme (Zeng et al., 2019).

Overall, the fractions for biphytanes synthesis in general (Eq. (5a), Fig. 3) are as follows (with x the degree of water exchange from 0% – minimal exchange, to 100% – maximal exchange):

$$\begin{aligned} n &= 80 - 2r \\ f_A &= \left[24 + \left(23 + \frac{1}{3} \right) (1 - x) - r \right] / n \\ f_{LSw} &= \left[\left(\frac{2}{3} \right) (1 - x) \right] / n \\ f_{RSw} &= r / n \\ f_{GGRw} &= (8 - r) / n \\ f_{LSNADPH} &= 16 / n \\ f_{GGRFAD} &= (8 - r) / n \\ f_x &= 24x / n \end{aligned} \quad (6a)$$

For *N. maritimus* and other organisms producing Ac-CoA autotrophically via the 3HP/4HB pathway, the water and NADPH fractions can be simplified to the terms from Eq. (5b):

$$f_{*W} = \frac{2}{3}f_{Aw} + f_{LSW} + f_{GGRW} + f_{RSW}$$

$$= \frac{16 + (15 + 5/9)(1-x) - (2/3)r}{n} + \frac{(2/3)(1-x)}{n} + \frac{8-r}{n} + \frac{r}{n} = \frac{24 + (146/9)(1-x) - (2/3)r}{80-2r}$$

$$f_{NADPH} = \frac{1}{3}f_A + f_{LSNADPH}$$

$$= \frac{8 + (7 + 7/9)(1-x) - (1/3)r}{n} + \frac{16}{n} = \frac{24 + (70/9)(1-x) - (1/3)r}{80-2r}$$

(6b)

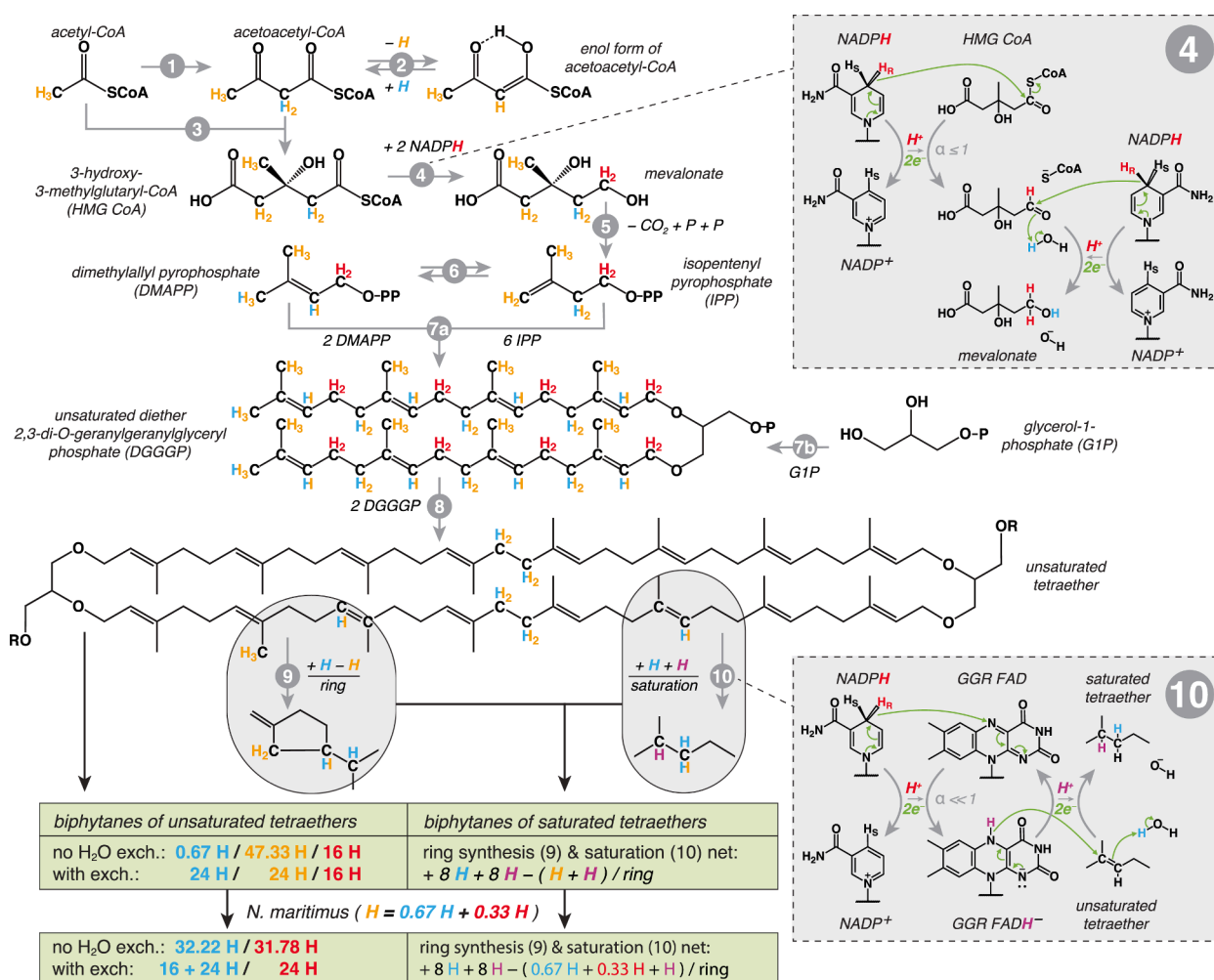


Fig. 3. Overview of H sources for archaeal tetraether biosynthesis. Here (orange) H from acetyl-CoA; (red) H from NADPH; (blue) H from protons (water-derived H⁺). Mixed potential sources of H from acetyl-CoA and water are shown half orange/half blue. For clarity, the H that enters lipid synthesis from acetyl-CoA methyl groups is visualized in orange; the biosynthetic sources of this H in *N. maritimus* are shown in Fig. S4. The summary box in green indicates the number of biphytane H that could originate from water during tetraether biosynthesis, which depends on the extent of re-equilibration during isomerization steps (2 & 6). See Tables 3, and Table S1 for full accounting. The net effect of ring formation on H sources combines the formation of the rings (step 9) with correspondingly fewer double bond reductions (step 10). The overall stoichiometry per ring for *N. maritimus* is a net of -0.67 H (blue) from water, -0.33 H (red) from NADPH and -1 H (purple) from the GGR flavin. The insets for steps 4 and 10 show the different hydride transfers. The GGR (step 10) is proposed to be highly fractionating. See the main text for further discussion. Biosynthetic steps are indicated in grey. 1: acetyl-CoA acetyl transferase; 2: tautomerization of acetoacetyl-CoA (can exchange the H at the C₂ position). 3: HMG CoA synthase; 4: HMG CoA reductase; 5: several alternative pathways from mevalonate to IPP (no H differences); 6: IPP isomerase (can exchange the H at the C₄ position); 7a: geranylgeranyl pyrophosphate synthase; 7b: geranylgeranyl glyceryl phosphate synthase; 8: tetraether synthase (Tes); 9: ring syntheses (GrsAB); 10: geranylgeranyl reductase (GGR).

Table 2

Changes in biosynthetic H source for ring-containing biphytanes relative to BP-0 for organisms producing Ac-CoA autotrophically via the 3HP/4HB pathway. Details in Table S1.

		$f^w + f_x$	f^{NADPH}	f_{FAD}
No water exchange	BP-1	+0.43%	+0.59%	-1.03%
	BP-2	+0.89%	+1.21%	-2.11%
	BP-3	+1.37%	+1.87%	-3.24%
Max. water exchange	BP-1	+0.68%	+0.34%	-1.03%
	BP-2	+1.40%	+0.70%	-2.11%
	BP-3	+2.16%	+1.08%	-3.24%

The full stoichiometry of BP isomers -0, -1, -2, and -3 is summarized in Table S1. In all cases, having more rings is equivalent to having fractionally more water-derived H^+ and NADPH-derived H^- , and less FAD-derived H^- (Table 2).

4.2. Hydrogen isotope flux balance model for archaeal biphytanes

Our quantitative model follows established approaches (e.g., Wijker et al., 2019). It divides the H isotope flux balance into two modules (Fig. 2):

- (1) *Total e-donor* pool of NADH from the exogenous electron donor with H transfer to NADPH (transhydrogenation).
- (2) *Biphytane synthesis* from water and the NADPH pool, plus the option to use GGR flavin-derived H^- (GGR-FAD) as an additional electron donor as explained in Section 4.1. For *N. maritimus* these are the only major sources of biphytane-H. For future analysis of heterotrophic archaea, this module also allows for incorporation of H directly from assimilated, rather than catabolized, organic substrates (arrow γ , not used for *N. maritimus*).

The H fluxes for *Biphytane synthesis* are set using the biosynthetic sources (Eqs. (5) and (6)). Solving the associated isotope budget for biphytane synthesis requires an estimate of the $^2H/^1H$ ratio of the NADPH pool, which is used throughout the cell and can have a variable isotope ratio depending on supply:demand, i.e., growth efficiency (Wijker et al., 2019). This necessitates solving the *Total e-donor* module separately to allow variation in the isotope ratio of the pool of NADPH. In autotrophic 3HP/4HB utilizing archaea, the only presumed source of NADPH is through an (as-yet unidentified) transhydrogenation reaction with NADH (Fig. 2A) generated by the electron transport chain during ammonia oxidation (Walker et al., 2010). In heterotrophs, the sources of NADPH, and therefore the potential effects on $^2H/^1H$ ratios of the NADPH pool, are more complex due to additional catabolic fluxes from organic precursors (Wijker et al., 2019; Zhang et al., 2009), which can also differ substantially between archaea and bacteria (Bräsen et al., 2014).

4.2.1. Total electron donor module – Determining flux and isotope balance for NADPH

To allow for growth-rate dependent effects, this module (Fig. 2B, upper half) permits reducing power (f_{ETC} , electron transport chain) to be recycled as a leakage flux, f_L (Eq. (7)). Modifying the approach of Wijker et al. (2019), we symbolize this not as excess NADPH production, but

rather an excess of electrons cycling through the $NADH \leftrightarrow NAD^+$ pool. Thus f_N , the production of NADPH co-factors from transhydrogenation of NADH, has a high fractional demand on f_{ETC} when the NADH supply (ammonia oxidation rate) is slow.

Mass balance, “*Total e-donor*” module:

$$f_{ETC} \equiv 1 = f_N + f_L \quad (7)$$

The unused reducing power, or leakage, is modeled as a function of the energy available to the cell according to a parameterization factor λ . Both a slow growth rate (high T_D) and a low value of λ (highly efficient cell) decrease f_L . The cell is thus growing with maximum efficiency ($f_L \rightarrow 0$) at the slowest, most energy-starved doubling time ($T_{D,max}$; where $X_{TD} = 1$) (Eqs. (8) and (9)).

Unused reducing power:

$$f_L = \lambda(1 - X_{TD}) \quad (8)$$

Growth rate dependence of f_L :

$$X_{TD} = \frac{T_D - T_{D-min}}{T_{D-max} - T_{D-min}}; f_L \downarrow \text{ as } T_D \uparrow \text{ and/or } \lambda \downarrow \quad (9)$$

Combining these equations yields the isotope balance for NADPH production in ammonium oxidizing archaea, where all f_i are fractional fluxes and all R_i are $^2H/^1H$ ratios (Eqs. (10) and (11)). Here, the $^2H/^1H$ ratio of NADPH is controlled by the fractionation relative to the electron donor pool (α_{ETC} , presumed to yield incoming NADH offset from water R_W), in combination with the fractionation associated with the unknown transhydrogenation process (α_{TH}). The magnitude of R_{NADPH} is related to R_{NADH} by a constant proportional offset ($R_{NADPH} = \alpha_{TH}R_{NADH}$), and R_{NADH} varies as a function of f_N . Note that these equations for cellular production of NADPH are not universal and would require metabolism-specific modifications if used for other autotrophs or heterotrophs, whereas the biphytane synthesis module is generalizable.

Isotope balance, “*Total electron donor*” module:

$$R_{NADH} = \alpha_{ETC}R_W / (\alpha_{TH} + \lambda(1 - X_{TD})(1 - \alpha_{TH})) \quad (10)$$

Then substitute:

$$R_{NADPH} = \alpha_{TH}R_{NADH} = \alpha_{TH}\alpha_{ETC}R_W / (\alpha_{TH} + \lambda(1 - X_{TD})(1 - \alpha_{TH})) \quad (11)$$

4.2.2. Biphytane synthesis module – Determining flux and isotope balance for BPs

The value of R_{NADPH} (Eq. (11)) is needed to calculate R_{BP} in the *Biphytane synthesis* module (Fig. 2B, lower half). We presume all water protons are governed by a common fractionation (α_W) and that all NADPH hydride sources have a single isotope effect (α_{NADPH}) during direct biosynthetic incorporation. The additional source of hydride from GGR reductants is symbolized by GGR-FAD (f_{FAD}), with a potentially different isotope effect (α_{FAD}) as detailed in the discussion. To allow for isomerization-related exchange of water protons, we include the variable f_x (“exchange”) with isotope effect α_x . The direct substrate flux, γ , would transmit unfractionated H directly from substrate to BPs in heterotrophs; it is not included here. The mass balance for biphytane synthesis then yields the full isotope balance:

Isotope balance, “*Biphytane synthesis*” module:

$$R_{BP} = (f^w\alpha_W + f_x\alpha_x)R_W + (f^{NADPH}\alpha_{NADPH} + f_{FAD}\alpha_{FAD})R_{NADPH} \quad (12)$$

Substitute Eq. (11) to obtain the isotope ratios of BPs:

$$R_{BP} = R_W \left[f^w\alpha_W + f_x\alpha_x + \left(f^{NADPH} + \frac{f_{FAD}\alpha_{FAD}}{\alpha_{NADPH}} \right) \left(\frac{\alpha_{NADPH}\alpha_{ETC}\alpha_{TH}}{\alpha_{TH} + \lambda(1 - X_{TD})(1 - \alpha_{TH})} \right) \right] \quad (13)$$

Table 3

Model results for KIEs α_W , α_{TH} , $\alpha_{ETC} \cdot \alpha_{NADPH}$, and $\alpha_{FAD}/\alpha_{NADPH}$, and flux coefficient λ ; proposed most likely scenario shown in bold. Errors represent standard error estimates from the non-linear least squares fit.

Parameter	Scenarios					
	$f_x = 0$			$f_x = \text{maximum}$		
H ₂ O exch. (f_x)						
α_W	0.5	0.7	0.9	0.5	0.7	0.9
$\alpha_{ETC} \cdot \alpha_{NADPH}$	1.148 ± 0.014	0.908 ± 0.015	0.669 ± 0.015	1.383 ± 0.020	0.983 ± 0.020	0.582 ± 0.020
$\alpha_{FAD}/\alpha_{NADPH}$	0.24 ± 0.06	0.25 ± 0.08	0.26 ± 0.10	0.15 ± 0.05	0.21 ± 0.07	0.35 ± 0.13
α_{TH}	0.22–0.57^a					
λ range	0.010–0.045	0.013–0.058	0.017–0.080	0.011–0.051	0.016–0.071	0.026–0.120
Ring effect	6.0–6.8‰ ring⁻¹					
Growth-rate effect	0.163–0.167‰ hr⁻¹					

^a Minimum and maximum KIE of hypothetical transhydrogenation, set as the limits of soluble and membrane-bound transhydrogenase KIEs reported in Wijker et al. (2019).

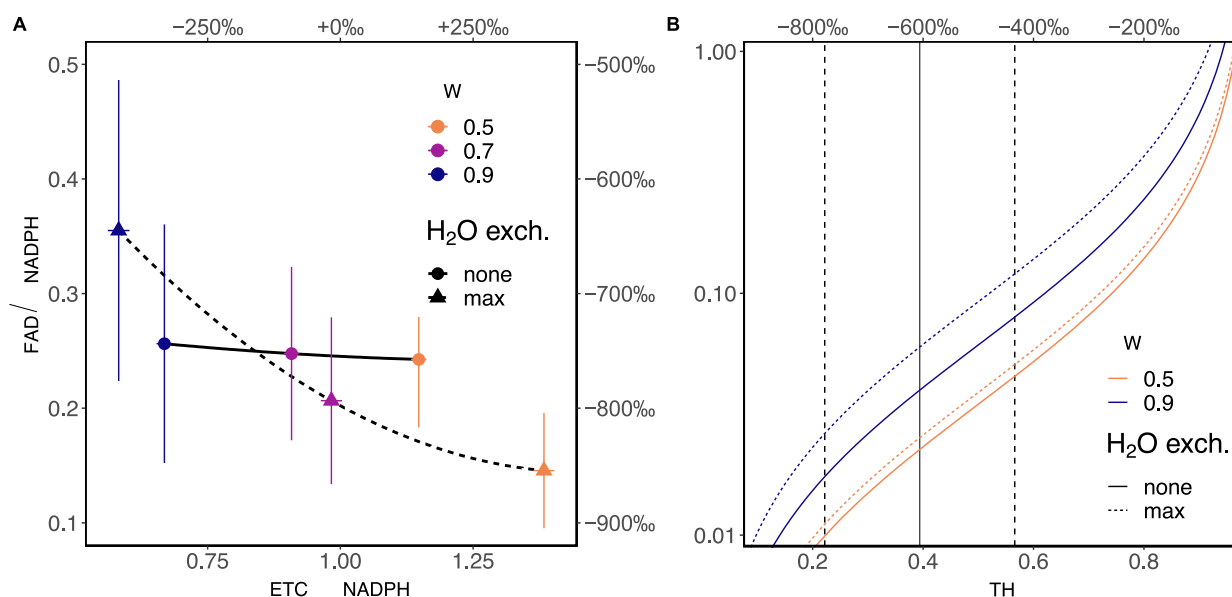


Fig. 4. Sensitivity analysis. The sensitivity of R_{BP} to model results. (A) Values of $\alpha_{FAD}/\alpha_{NADPH}$ vs. $\alpha_{ETC} \cdot \alpha_{NADPH}$ at different levels of water exchange (f_x , none or maximum) and α_W show the relative insensitivity and strong fractionation of α_{FAD} relative to the other terms. Error bars represent standard error estimates from the non-linear least squares fit (see Table 3). At the consensus values of $\alpha_W = 0.9$ and $f_x = 0$, $\alpha_{ETC} \cdot \alpha_{NADPH} = 0.669$ and $\alpha_{FAD}/\alpha_{NADPH} \approx 0.25$. (B) The co-dependence of α_{TH} and λ indicates the minimum likely value of α_{TH} is > 0.22 boundary value (from PntAB), and that the data only would be compatible with values of $\alpha_{TH} > 0.57$ (from sTH) if λ were > 0.1 ; the consensus range of λ is 0.02–0.08 (Table 3). Error envelopes represent standard error estimates from the non-linear least squares fit.

While Eq. (13) may describe the values and patterns for the $^2\text{H}/^1\text{H}$ ratios of biphytanes, it contains seven unknowns: λ and all six isotope effects, α_i . The problem is reducible, however, through a combination of supported assumptions and by having data for multiple biphytanes, each at several different growth rates. These controlled variants impart predictable changes to the stoichiometric fractions, f_i , yet the corresponding values of R_{BP} must be satisfied using a single set of KIEs unique to the organism. Additionally, the model must account for the observation that cyclopentane rings increase the $^2\text{H}/^1\text{H}$ ratio in response to shifts among the fractional hydrogen sources (Table 2). Cyclopentane rings are formed by GrsAB as an alternative to saturation by GGR, and therefore it may be informative to view the pattern from the opposite perspective: every GGR-mediated reduction ($\text{H}^- + \text{H}^+$) decreases $^2\epsilon_{L/W}$ by -6.4% . To examine this idea, we implemented a least-squares optimization routine to estimate all values of α_i and examine the results in the context of these data patterns.

4.2.3. Model solutions, *N. maritimus*

Data for the four BPs and three growth conditions ($T_{D-\text{min}}$ and $T_{D-\text{max}}$ assumed to be 20 h and 120 hr; (Könneke et al., 2005; Santoro and

Casciotti, 2011)) were fit using the following assumptions: $\alpha_W = \alpha_x = 0.5$; 0.7; or 0.9 and $f_x = 0$ (no water exchange) or $f_x = 30\%$ (maximal water exchange during lipid biosynthesis). With these assumptions, there are four remaining unknowns:

λ	leakiness of the electron donor flux
α_{TH}	isotope effect of NADPH/NADH transhydrogenation
$\alpha_{ETC} \cdot \alpha_{NADPH}$	the product of α_{ETC} and α_{NADPH}
$\alpha_{FAD}/\alpha_{NADPH}$	the ratio of α_{FAD} to α_{NADPH}

When the least squares model fit is calculated using values of α_W (and α_x) that are significantly smaller than 0.9, the other KIEs (α_i values) would become >1 to compensate, i.e., have inverse isotope effects (Table 3, Fig. 4). We suggest our results for *N. maritimus* are more likely to resemble prior work which has consistently yielded estimates of $\alpha_W \approx 0.9$ (Wijker et al., 2019; Zhang et al., 2009) but also note that moderate changes in the value assigned to α_W and α_x affect the absolute values of the model outcomes but do not affect the relative patterns (Fig. 4). Likewise, changes in water exchange (f_x) affect the absolute values of λ and the KIEs but not the overall patterns considering the error estimates of the parameter estimates. Overall, we consider a high degree of water exchange to be unlikely given the metabolic efficiency and likely close

coupling of biosynthetic steps in *N. maritimus*.

The values of α_{ETC} and α_{NADPH} cannot be determined independently because their product occurs in the numerator of a single term (Eq. (13)). With $\alpha_{\text{W}} = 0.9$, the fit to the data shows the optimal value of $\alpha_{\text{ETC}} \cdot \alpha_{\text{NADPH}}$ to be tightly constrained (0.669 ± 0.015 without water exchange; 0.582 ± 0.020 with maximal exchange; Table 3) regardless of the values of the other parameters. The relatively large value of this product implies that neither of the individual KIEs is likely to be highly fractionating. If one of these α values is 0.90, the other would be 0.74 without water exchange and 0.65 with maximal exchange; if equal, they are each 0.82 and 0.76, respectively. These results are less fractionating than current estimates for bacterial transhydrogenases (PntAB; Wijker et al., 2019). The process symbolized by α_{ETC} , however, is not transhydrogenation, but rather the net fractionation associated with the transfer of H from the inorganic electron donor via membrane-bound respiratory complex 1 (e.g., NDH1, a.k.a. Nuo; Walker et al., 2010) (Fig. 2A). To our knowledge, the specific hydrogen KIE for enzymes such as NDH1 have not been characterized, nor any net fractionations for H transfer by any known membrane-bound respiratory complex.

Regardless of how the components of $\alpha_{\text{ETC}} \cdot \alpha_{\text{NADPH}}$ are defined, the solution for $\alpha_{\text{FAD}}/\alpha_{\text{NADPH}}$ indicates the GGR-FAD reduction step (α_{FAD}) is much more strongly fractionating than either α_{ETC} or α_{NADPH} . The least-squares best-fit value for $\alpha_{\text{FAD}}/\alpha_{\text{NADPH}}$ is tightly constrained ranging from 0.24 to 0.26 when water exchange is minimal (Table 3); an independent Monte Carlo simulated annealing approach likewise yielded 0.24 ± 0.11 . The mean of these approaches (0.25) is equivalent to ${}^2\varepsilon_{\text{FAD}}/{}^2\varepsilon_{\text{NADPH}} \approx -750\text{‰}$ (Fig. 4A, Table 3), and thus if $\alpha_{\text{NADPH}} = 0.7\text{--}0.9$, $\alpha_{\text{FAD}} = 0.18\text{--}0.23$ (${}^2\varepsilon_{\text{FAD}} \approx -770$ to -820‰). Even for the scenario with maximal water exchange during lipid biosynthesis (Table 3) ${}^2\varepsilon_{\text{FAD}}/{}^2\varepsilon_{\text{NADPH}} \approx -650\text{‰}$ and ${}^2\varepsilon_{\text{FAD}} \approx -690$ to -760‰ . Our estimate for α_{FAD} thus resembles, but is potentially even more strongly fractionating than, the results for GGR-mediated, step-wise saturation of geranylgeraniol to phytol in cucumber (mean $\alpha_{\text{GGR}} = 0.303$, or -697‰ ; Chikaraishi et al., 2009). Chikaraishi and colleagues estimated ${}^2\text{H}/{}^1\text{H}$ ratios for the hydrogens added during saturation of geranylgeraniol to dihydrogeranylgeraniol ($-649 \pm 92\text{‰}$), to tetrahydrogeranylgeraniol ($-728 \pm 81\text{‰}$), and ultimately to phytol ($-715 \pm 79\text{‰}$).

The remaining unknowns are λ and α_{TH} , and again there is no unique solution (Eq. (13)). However, every optimized combination of λ and α_{TH} must both reproduce the ring-dependence of the isotope composition of the individual BPs and show the observed sensitivity (slope, ‰ hr^{-1}) of ${}^2\varepsilon_{\text{L/W}}$ to changes in growth rate. These relationships are visualized in Fig. 4B, which illustrates the interdependence of these two variables. Assuming the value of α_{TH} falls within the range of prior reports for soluble (sTH, $\alpha = 0.566$; (Wijker et al., 2019)) and/or membrane bound (PntAB, maximum fractionation endmember $\alpha = 0.222$; (Jackson et al., 1999; Wijker et al., 2019)) transhydrogenases, this implies the value of λ must be < 0.12 even with maximal water exchange (Table 3). Because λ determines the “leakiness” (Eq. (8)), this implies $f_{\text{L}} = \lambda(1 - X_{\text{TD}}) < 0.12$.

Overall, the strong ${}^2\text{H}$ discrimination of α_{FAD} implies that the value of R_{BP} is minimally sensitive either to α_{NADPH} or α_{W} , including in cases where water exchange (f_{x}) is non-zero (Fig. 4A). This analysis also shows that highly fractionating values of α_{W} lead to unreasonably high estimates for the value of α_{ETC} (assuming $\alpha_{\text{NADPH}} < 1$). The high sensitivity to λ also shows how the results are relatively insensitive to the chosen value of α_{TH} . For example, if α_{TH} is > 0.5 , i.e., more similar to sTH than PntAB (Fig. 4B), λ is ~ 0.08 . Alternatively, if α_{TH} is set to the mid-point (0.394), λ is 0.04. Regardless of the exact value, all reasonable solutions imply the value of λ must be small (Table 3), which is consistent with the observation that ${}^2\varepsilon_{\text{L/W}}$ of *N. maritimus* biphytanes responds insignificantly to changes in cell growth rate. Such a result also agrees with the concept that Archaea are optimized for energy-limited conditions (Valentine, 2007), implying that nearly all reducing power (NADH derived from the e^- donor) is allocated to obligatory cellular needs. At the estimate of $\lambda = 0.04$ and a mid-point of $T_{\text{D}} = 56$ hr, the value of $f_{\text{N}} = 98\%$ (Eq. (8) and (9)), i.e., only 2% of produced NADH is lost (f_{L}). A 98% value for f_{N} represents the electron flux that is harvested from NADH into the NADPH pool and obligately dedicated to the full suite of cellular metabolic fates, only part of which is lipid synthesis. If this conceptual framework is robust, it would be difficult to change the isotopic composition of NADPH due to effects around the f_{N} vs. f_{L} branch point (Hayes, 2001), and ${}^2\varepsilon_{\text{L/W}}$ should be insensitive to growth rate (and perhaps energy flux), not only in AOA, but potentially in all autotrophic archaea.

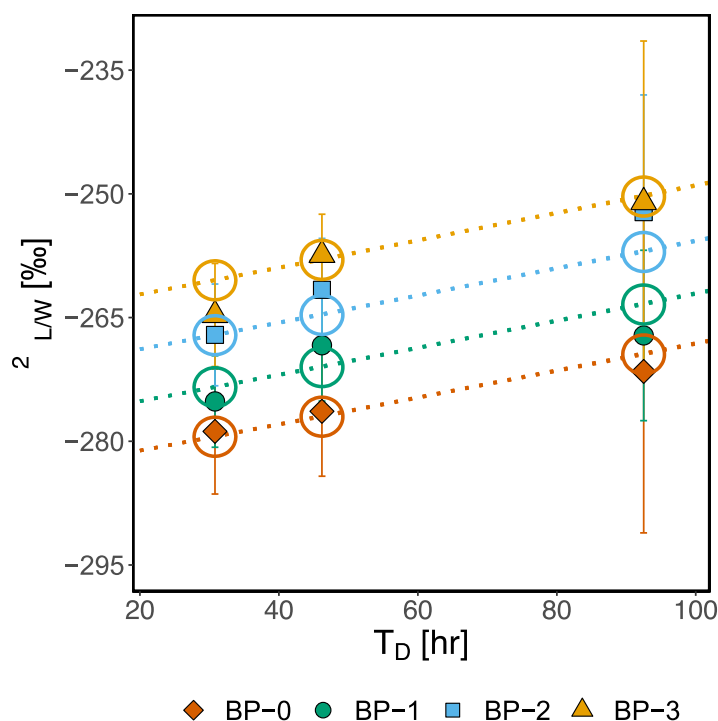


Fig. 5. Model/data comparison. The ${}^2\varepsilon_{\text{L/W}}$ values for BPs of *N. maritimus* from models and measurements, showing growth-rate and ring-number dependence. Open symbols are the model fit simulation while closed symbols are the data; calculations use the consensus estimates of kinetic isotope effects (Table 3). The growth-rate effect, or slope of ${}^2\varepsilon_{\text{L/W}}$, from all model fits ranges from 0.163 to 0.167 ‰ hr^{-1} (the data yield $0.18 \pm 0.09\text{‰ hr}^{-1}$; Fig. 1). The ring-dependent enrichment of ${}^2\text{H}$ from all model fits ranges from 6.0 to 6.8 ‰ ring^{-1} (the data yield $6.4 \pm 2.7\text{‰ ring}^{-1}$).

The final estimated solutions (Table 3) reproduce the three major features of the ${}^2\epsilon_{L/W}$ data for *N. maritimus* biphytanes: (i) highly ${}^2\text{H}$ -depleted absolute values, (ii) relative insensitivity to changes in growth rate, and (iii) the increase in isotope ratio with ring number. Specifically, all model fits yield an increase between 6.0 and 6.8‰ per ring, compared to the +6.4‰ per ring observed for the data, and yield a small positive slope (0.163–0.167‰ hr^{-1}) of ${}^2\epsilon_{L/W}$ versus T_D (Table 3; Fig. 5). Most of the ring-associated increase is attributed to the large KIE of the FAD-based hydride transfer for GGR, while the relatively shallow growth-rate slope reflects the small value of λ , which likely reflects inflexible physiological fluxes in *N. maritimus*.

5. Discussion

The motivation for this work was to investigate the potential of ${}^2\text{H}/{}^1\text{H}$ ratios of archaeal lipids as archives of past environments, ecologies, or physiologies. In sharp contrast to the >600‰ range of values observed across the bacteria (Osburn et al., 2016; Valentine et al., 2004; Wijker et al., 2019; Zhang et al., 2009), the archaea stand out for their narrow apparent span of ${}^2\epsilon_{L/W}$ values (Dirghangi and Pagani, 2013; Kaneko et al., 2011; Lengger et al., 2021; Wu et al., 2020). This is somewhat unexpected, given the diversity of species, growth substrates, and metabolic strategies among the archaeal taxa studied to-date (e.g., *Sulfolobus* sp., *Methanosarcina barkerii*, *Nitrosopumilus maritimus*). Archaeal lipids are generally ${}^2\text{H}$ -depleted, and therefore sit at the lower end of the range previously reported for fatty acids from aerobic heterotrophic bacteria (Sessions et al., 2002; Valentine et al., 2004; Campbell et al., 2009; Zhang et al., 2009; Heinzlmann et al., 2015; Leavitt et al., 2016a,b, 2017; Osburn et al., 2016), and are similar to values from acetogens and some sulfate reducers (Campbell et al., 2009; Osburn et al., 2016; Valentine et al., 2004). Perhaps most striking is the consistency between our findings for ${}^2\epsilon_{L/W}$ archaeal biphytanes and the experimental observations for phytol/water from cucumber ($-345 \pm 3\%$) (Chikaraishi et al., 2009), phytol/water in *E. huxleyi* cultures ($-344 \pm 23\%$) (Sachs et al., 2016), and the range of phytol values recovered from recent marine sediment (Li et al., 2009).

Our results for *N. maritimus* show that its BPs are generally more ${}^2\text{H}$ -depleted (low ${}^2\epsilon_{L/W}$ values of -257% for BP-3 to 279% for BP-0) than the range of ${}^2\epsilon_{L/W}$ values from the heterotrophic and halophilic archaeon *Haloarcula marismortui*, which yielded archaeol/water ${}^2\epsilon_{L/W}$ values of -103 to -228% (Dirghangi and Pagani, 2013). *N. maritimus* also appears more ${}^2\text{H}$ -depleted than batch cultures of an aerobic heterotroph *Sulfolobus* spp. (also a hyperthermoacidophile), where ${}^2\epsilon_{L/W}$ values ranged from -213 to -161% for BP-0 to -4 (Kaneko et al., 2011); whereas intact GDGT-1 and -2 from *Sulfolobus solfataricus* showed average ${}^2\epsilon_{L/W}$ values around -134% (Lengger et al., 2021). The differences between ${}^2\epsilon_{L/W}$ for BPs vs. GDGTs likely derive from the glycerols in GDGTs, and secondarily, to differences in the experiments and strains between the two studies (Kaneko et al., 2011; Lengger et al., 2021). The values we observe for *N. maritimus* are similar to the range for *Methanosarcina barkerii*, which yielded ${}^2\epsilon_{L/W}$ from -204 to -322% for phytanes, depending on methanogenesis substrate (Wu et al., 2020). *N. maritimus* expresses simple patterns of ${}^2\epsilon_{L/W}$ values, where the dominant feature is a dependence on the number of rings, with the lowest values in BP-0, increasing up to BP-3 (Fig. 1). The weak sensitivity of ${}^2\epsilon_{L/W}$ to changes in electron-donor limited growth rate stands in contrast to the response of fatty acids from bacteria grown with similar strategies (Kopf, 2015; Kopf et al., 2015; Leavitt et al., 2019). The model developed above (Section 4) explored how these patterns can help distinguish the H sources for BP biosynthesis and enabled estimation of key KIEs. The limited growth rate sensitivity implies that *N. maritimus* maintains a relatively consistent H-balance or cellular redox budget, regardless of electron donor flux and growth rate. This implicates a constant baseline $\delta^2\text{H}$ signature as a feature of relatively imperturbable central energy metabolism. This interpretation may also explain the observations in autotrophic sulfate reducing bacteria (Osburn et al.,

2016). Stepping beyond this experimental and model framework, we now look toward physiological inferences and paleoenvironmental applications.

5.1. Biochemical drivers of ${}^2\epsilon_{L/W}$ patterns

5.1.1. Sources of cofactor hydrogen for lipid synthesis in 3HP/4HB utilizing Archaea

N. maritimus is an obligate chemoautotroph that utilizes the 3HP/4HB pathway for carbon fixation (Kim et al., 2016; Bayer et al., 2019; Könneke et al., 2014). Because all biphytane-bound H in the present experiments is strictly biosynthetic, rather than assimilated as part of an organic substrate, the observed differences in ${}^2\epsilon_{L/W}$ values between individual BPs (Fig. 1) must be primarily due to different KIEs associated with hydride transfer reactions. As such, the patterns we observed here may be expressed differently in heterotrophic archaea or during mixotrophic growth.

In the model framework developed here, the overall mean value for ${}^2\epsilon_{L/W}$ in *N. maritimus* reflects primarily the expression of $\alpha_{\text{ETC}}\alpha_{\text{NADPH}}$ (0.669; equivalent to $\sim -330\%$) modulated by the incorporation of water ($\alpha_{\text{W}} = 0.9$; equivalent to -100%), while the ring-based difference is controlled by the stoichiometric balance and the KIE associated with GGR (α_{FAD}). This implies that the magnitude of ${}^2\epsilon_{L/W}$ would likely be expressed differently in heterotrophic archaea but biphytanes could still show ring effects from the use of GGR. This may help to explain why our results are similar, yet not equal, to prior data from *Haloarcula marismortui* and *Sulfolobus* spp. (Dirghangi and Pagani, 2013; Kaneko et al., 2011). These prior data also were not obtained on steady-state cultures, which may be an additional factor contributing to the observed differences. Additionally, in heterotrophic aerobic archaea (e.g., *Sulfolobus* species), glucose dehydrogenase and potentially glyceraldehyde dehydrogenase from the Entner-Doudoroff pathway are likely major contributors of NADPH (Bräsen et al., 2014; Nunn et al., 2010), potentially with an impact on the final ${}^2\epsilon_{L/W}$ signature.

The most definitive result of our modeling approach is the prediction of a highly ${}^2\text{H}$ -depleted hydrogen supplied by GGR-FAD during saturation of DGGGP (Fig. 3). Our prediction, in combination with results from the phytol of plants (Chikaraishi et al., 2009), point towards a relatively constant KIE for the GGRs across at least two, and perhaps all domains of life, despite differences in GGR reduction mechanisms. As discussed in section 4.1.1, the FAD in GGRs of cyanobacteria and plants (*Synechocystis* and *Arabidopsis* spp.) is directly reduced by NADPH in a hydride-transfer reaction (Addlesee et al., 1996; Keller et al., 1998) and although the GGR in cell extracts of some archaea (*Thermoplasma acidophilum*) also seem to work by this type of hydride transfer (Nishimura and Eguchi, 2006), others (e.g. *Sulfolobus acidocaldarius* and *Archaeoglobus fulgidus*) have been speculated to require F_{420} or Fd as *in vivo* reductants (Murakami et al., 2007; Sato et al., 2008). At the same time, *in vitro* experiments at non-physiological concentrations of NADH (>10 mM) with FAD also led to minor GGR activity in *S. acidocaldarius* (Sasaki et al., 2011). The most convincing evidence that Fd can provide electrons to reduce the flavin in GGR in some archaea comes from the heterologous expression and activity of *Methanosarcina acetivorans* GGR (Ma-GGR) in *E. coli*. In these experiments, Ma-GGR were active only when native Ma-Fd was co-expressed (Isobe et al., 2014). Similar work in *S. acidocaldarius* showed activity for Sa-GGR in *E. coli* without Sa-Fd, although native *E. coli* Fd and NADPH:ferredoxin oxidoreductase were present (Sato et al., 2008). This is also consistent with evidence that Fd-dependent, flavin-NAD complexes may be the favored electron-shuttling cofactors in chemo(litho)autotrophs (Buckel and Thauer, 2018; Boyd et al., 2020)(Nishimura and Eguchi, 2006).

In AOs including *N. maritimus*, the *in vivo* reductant of the GGR-bound FAD remains unknown. However, the ferredoxin-NADP⁺ reductase (FNR) gene is highly conserved among both the pelagic marine and terrestrial AOs (Ren et al., 2019). Taken together with the *in vivo* and *in vitro* experiments on other archaeal GGRs discussed above, FNR is a

plausible candidate for providing the redox cofactor that reduces the GGR flavin in *N. maritimus* (Fig. 2A) (thereby resembling *M. acetivorans*). If reduced Fd is the source of electrons for NADPH, this also means a water-derived proton is required to generate a functional hydride that is transferred onto the GGR-FAD, and ultimately to the GDGT and our observed BP. Regardless of the ultimate source of donor electrons and H, archaeal GGRs utilize a flavin (FAD) cofactor for DGGP saturation (Nishimura and Eguchi, 2006; Sasaki et al., 2011). Thus, for *N. maritimus* we model NADPH as the reductant for the FAD in GGR with isotope effect α_{FAD} ($=0.18$ – 0.23), which we speculate is similar to the mechanism and KIE of phytol saturation (Chikaraishi et al., 2009). The mechanism for this strong H-KIE in GGR is unknown but it is conceivable that a hydrogen tunneling based hydride transfer mechanism (Cha et al., 1989; Nagel and Klinman, 2006) from NADPH to the GGR flavin is at play. Such H-tunneling effects have been discovered in other flavoenzymes such as pentaerythritol tetranitrate reductase where flavin reduction by NADPH has a primary kinetic isotope effect of ~ 0.14 (-860%) (Pudney et al., 2009b,a).

Synthesis of GDGTs also requires hydrides donated directly from NADPH, both during synthesis of acetyl-CoA (Fig. S4) and later, during polyisoprene synthesis of DGGGP (Fig. 3, steps 1–7). *N. maritimus* and other AOAs, however, likely generate NADH via NADH:ubiquinone oxidoreductase (Nuo = NDH1) rather than NADPH. This would necessitate *N. maritimus* to produce NADPH for anabolism by other means (Spaans et al., 2015), possibly by as-yet unidentified transhydrogenase (s), as assumed in our metabolic model, or via the above mentioned FNR. In bacteria, the biosynthetic NADPH pool is regenerated by transhydrogenation from NADH, and thus sources its reducing power directly from the primary supply generated by the electron transport chain (Fuhrer and Sauer, 2009; Sauer et al., 2004). In most bacteria this process is catalyzed by transhydrogenase (TH) enzymes that transfer the hydride (H^-) between NADH and NADP^+ as needed to replenish deficits as NADPH hydrides are consumed during anabolism (biosynthesis) (Sauer et al., 2004). The hydride transfer reaction by bacterial TH enzymes are associated with a strong ^2H discrimination ($^2\varepsilon_{\text{TH}} = -778$ to -434% ; Jackson et al., 1999; Wijker et al., 2019). While homologues of bacterial THs are seen in some methanogens, they are otherwise rare in Archaea (c.f. Buckel and Thauer, 2013, 2018; Leavitt et al., 2016a; Poudel et al., 2018). Consistent with this rarity, we were unable to find

homologues to common bacterial (e.g., *E. coli* or *D. alaskensis*) soluble or membrane-associated transhydrogenases in the *N. maritimus* genome (Table S2). *N. maritimus*, like other archaea, does encode other mechanisms to balance its intracellular redox budget (Spaans et al., 2015) – such as ferredoxin-dependent, as well as Fe-free flavin-NAD flavodoxin complexes, and Cu-binding plastocyanin-like proteins (Shafiee et al., 2022). Known and identified NADPH producing enzymes annotated in the *N. maritimus* genome are summarized in Table S2. The main NADPH sources not associated with central carbon metabolism include a cytosolic NADP^+ -reducing hydrogenase (SH; Nmar_0253, Nmar_0267, Nmar_1389), and the above-mentioned ferredoxin: NADP^+ oxidoreductase (FNR; Nmar_0672). Sources of NADPH coupled to the TCA cycle are IDH (Nmar_1069, Nmar_1379), and a NADP^+ glyceraldehyde dehydrogenase (Nmar_1608) coupled to the non-phosphorylating Entner Doudoroff pathway. We are unable to speculate on the specific mechanism of transhydrogenation present in *N. maritimus* but note that the isotope fractionation (α_{TH}) we require is in the range of bacterial values (Fig. 4, Table 3). Moreover, α_{TH} is not highly expressed in this model, due to the nearly completely quantitative flux through the NADH pool to the NADPH pool (i.e., the value of f_{N} approaches 1). It is therefore more informative to note that this approach places hard constraints on the maximum value of λ and indicates there are no permitted solutions that enable significant energy waste (lost NADH, f_{L}) in *N. maritimus*. Regardless, a better understanding of the precise mechanism(s) by which *N. maritimus* interconverts $\text{NADH} \leftrightarrow \text{NADPH}$, or how it may generate NADPH directly during catabolism, is vital towards gaining a more mechanistic understanding of the $^2\varepsilon_{\text{L/W}}$ signatures encoded in its lipids.

5.1.2. Interpreting metabolic limits on $^2\varepsilon_{\text{L/W}}$ values

In the framework set forth by Wijker et al. (2019) for bacteria, we model *N. maritimus* as having an NADPH imbalance flux of -100% . Our best fit estimate for $\lambda = 0.04$ (range 0.01 – 0.12 ; Table 3) equates to 98% of the electron flux through NADH being used for NADPH generation and only 2% in “excess” for recycling or leakage. We then model NADPH as being entirely consumed for cellular processes with no loss from NADPH back to NADH. This framework is consistent with our isotope data, which place *N. maritimus* at a negative NADPH imbalance in the Wijker et al. (2019) reference frame (Fig. 6). Accounting for the 95%

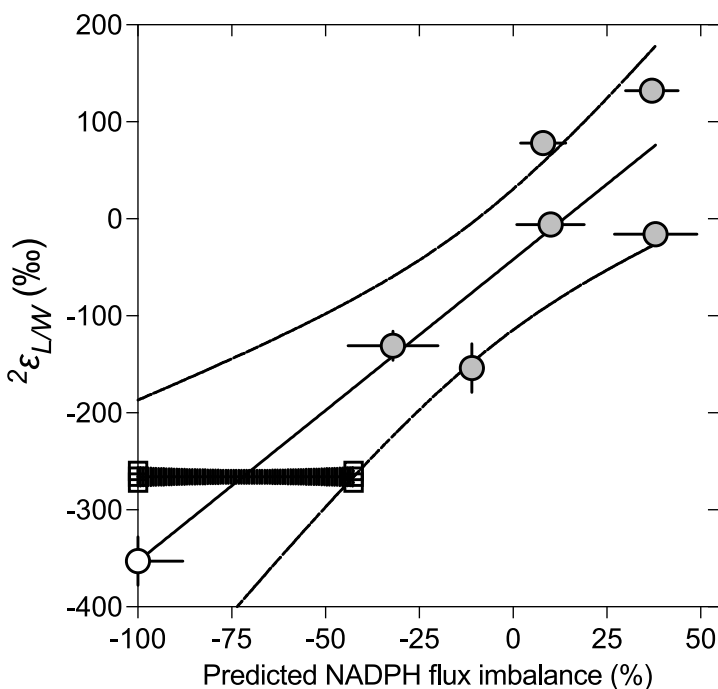


Fig. 6. NADPH flux imbalance. NADPH flux imbalance, f_{L} . The $^2\varepsilon_{\text{L/W}}$ values bacterial $^2\varepsilon_{\text{L/W}}$ (grey circles) versus NADPH availability (Wijker et al., 2019). From this we calculated and plot a linear regression and 95% confidence interval (solid and dashed lines) derived from the Wijker et al. (2019) dataset forced through the y-intercept at -100% flux imbalance (open white circle). We then plot the measured $^2\varepsilon_{\text{L/W}}$ from *N. maritimus* (open squares, y-values only) showing the minimum and maximum possible NADPH flux imbalance, -100 and -42% , respectively (horizontal black bar), extrapolated from the 95% CI from the bacterial work. This example is illustrative and may not reflect the true flux imbalance in *N. maritimus*.

confidence intervals on a linear regression of the Wijker values, *N. maritimus* $^{2}\epsilon_{L/W}$ falls within the expected limits of bacterial lipid synthesis. It remains unknown whether this also is a reasonable approximate minimum value for $^{2}\epsilon_{L/W}$ for bacterial production, or whether the ~200‰ scatter in the y-intercept (at -100% NADPH; Fig. 6) portends a large range for the projected minima of diverse energy-limited organisms, for example, autotrophic sulfate-reducing or acetogenic bacteria (Campbell et al., 2009; Osburn et al., 2016; Valentine et al., 2004), and other autotrophic archaea (e.g. Wu et al., 2020). A possibility that requires further investigation is whether free energy differences are primarily responsible for changes in $^{2}\epsilon_{L/W}$ (changes in the intercept) at a given NADPH imbalance. If so, more experiments at constant energy flux (e.g. chemostats) for organisms with distinct metabolisms will help define this space, and the outcome may reflect thermodynamic properties of the experiments (Amenabar et al., 2017; Boyd et al., 2020).

Any potential contributions from equilibrium isotope exchange in various reaction steps also remain unknown. Such effects could be examined by cultivation at different temperatures and different starting water compositions, again across steady-state growth rates. Thus, while we do not know how the $^{2}\epsilon_{L/W}$ observed here (with *N. maritimus*, isothermally at 28 °C) relates to the maximum isotope effect of a unidirectional H⁻ donation (kinetic effect), or whether there is H⁻ isotopic exchange at equilibrium, we infer that isoprenoid biosynthesis shares common net fractionations values with other microbial lipids, as expressed in accordance with cellular energy balance and fluxes (Wijker et al., 2019). Theoretical calculations of the equilibrium isotope effect (EIE) for an idealized linear isoprenoid versus water yielded an estimate of -100‰, and was insensitive to temperature over 0 to 100 °C (Wang et al., 2009). This is effectively the same as what we assigned empirically ($\alpha_w = 0.9$) and suggests the water-derived isotope component of the net BP biosynthesis isotope values will not respond to biological temperature variations, although this remains to be experimentally verified. Together these examples suggest that any EIE component of the $^{2}\epsilon_{L/W}$ signals of Nitrososphaerota BPs should be insensitive to temperature, in addition to their insensitivity to growth rate.

5.2. Applications

5.2.1. Calibrating biphytane $^{2}\epsilon_{L/W}$ offsets for paleohydrology and paleoecology

Archaeal lipids may offer some unique advantages as H isotope paleohydrologic proxies. The iGDGTs found in aquatic sediments are believed to derive predominantly from marine or lacustrine ammonia-oxidizing archaea living in the overlying water column and thus are dominantly aquatic biomarkers (Powers et al., 2010; Pearson and Ingalls, 2013; Schouten et al., 2013). This contrasts with sedimentary leaf wax-derived *n*-alkanes, which can derive from a complex and dynamic plant community, may be contributed by both terrestrial and aquatic plants with differing growth water (i.e. soil and lake water, respectively), and have seasonally-biased production in some regions (Gao et al., 2011; Sachse et al., 2012; Tipple et al., 2013; McFarlin et al., 2019) and thus lean on additional proxy data to inform interpretation of trends in sedimentary $\delta^2\text{H}_{\text{wax}}$ through time. In lacustrine bodies with minimal terrigenous overprinting, it may be possible to reconstruct the water $\delta^2\text{H}$ composition from archaeal biphytanes and an estimated constant $^{2}\epsilon_{L/W}$ value, using either a mean value or individual BP-specific values. Tandem work on modern lake core-tops over a range of temperature regimes may provide an indication of the magnitude of any temperature effects, although it remains unknown whether this archaeal $^{2}\epsilon_{L/W}$ offset is temperature sensitive (see section 5.1.2). Once calibrated, the reconstructed lake water record could be compared to estimated regional meteoric water $\delta^2\text{H}$ values obtained from co-deposited *n*-alkanes (Tipple et al., 2013), potentially yielding insights to past changes in the hydrologic cycle or physiological effects that can be missing from the plant perspective (Sachse et al., 2012). This may help reveal diverse

GDGT sources in some lacustrine systems when paired with C-isotopes (Sinninghe Damsté et al., 2022). In today's oceans variation in the $\delta^2\text{H}$ value of water is minimal, and a modern core-top calibration of $\delta^2\text{H}_{\text{GDGT}}$ may enable us to calibrate temperature signals independently from variations in source water. Separately, if high precision marine $\delta^2\text{H}_{\text{GDGT}}$ records were reconstructed through a suite of glacial/interglacial times periods, such observations may help constrain the temperature/ice volume problem that exists for bulk $\delta^{18}\text{O}$ records in marine carbonates, independently from clumped carbonate Δ_{47} (Eiler, 2011; Epstein et al., 1951; McCrea, 1950), enabling new lines of inquiry. Both types of calibration efforts likely will be needed. While GDGT hydrogen isotope measurements remain technically challenging, particularly on intact GDGTs (Lengger et al., 2021), improvements in methodology will make these more routinely accessible in the future.

Variations in salinity have ca. 50‰ effects on the $^{2}\epsilon_{L/W}$ values of alkenones from haptophyte algae (Sachs et al., 2016; Schouten et al., 2006; Weiss et al., 2017). The mechanism by which salinity affects $^{2}\epsilon_{L/W}$ values in haptophytes remains unclear. Within non-photosynthetic bacteria or archaea, we found only one study where salinity is tested in a heterotrophic halophilic archaeon, where both growth rate and $^{2}\epsilon_{L/W}$ changed with salinity shifts, with larger fractionations at faster rates (Dirghangi and Pagani, 2013). Perhaps the small change in $^{2}\epsilon_{L/W}$ value was linked to NADPH's role in the universal stress response, or due to a confounding effect on growth rate. Differences in salinity and taxonomy produce different iGDGT assemblages among Nitrososphaerota (Elling et al., 2015; 2017), which would then yield differences between taxa in their bulk average $^{2}\epsilon_{L/W}$ values to be consistent with the pattern of increasing $^{2}\epsilon_{L/W}$ for BP-0...BP-3. However, estimates of the net effect of such changes based on variation in Ring Index suggests that the effect would be minimal (<10‰), even between the very high Ring Index composition of *Nitrososphaera gargensis* (BP-0:1:2:3 ratio of 0.02:0.02:0.51:0.45; calculated by Elling and colleagues by assuming iGDGT-2 consists only of 2 × BP-1 (Elling et al., 2017)) vs. the BP distribution in *N. maritimus*. Thus, the taxonomic influence of iGDGT compositional changes on average $^{2}\epsilon_{L/W}$ values of BP assemblages should be insignificant. Whether $^{2}\epsilon_{L/W}$ values are influenced by salinity independently of changes in ring distribution requires further investigation. It may be likely that regional variations would overwhelm any salinity effects or taxonomic community shifts in the evaluation of either lacustrine or marine biphytane $\delta^2\text{H}$ proxies. For applications in freshwater lacustrine, riverine sediments, and perhaps springs, salinity is often less of concern, where alternatively, proxies in these settings should be examined for potential pH effects. In some more extreme environments (e.g. salars, brines, hot springs), the role of pH, salinity, and even water activity, on archaeal $^{2}\epsilon_{L/W}$ may prove a useful proxy of archaeal activity.

Growth rates of natural microbial communities can vary spatially and temporally, depending on the availability of nutrients, electron donors and acceptors, temperature, and other environmental parameters. The conditions used in this work were designed to test a broad range of metabolic rates at controlled steady state. We anticipated that variations in energy budgets associated with fast and slow growth would yield heterogeneity of $^{2}\epsilon_{L/W}$ values analogous to the differences in $^{2}\epsilon_{L/W}$ values of bacteria grown aerobically on different hexoses (Wijker et al., 2019), or haptophyte algae grown at different rates by varying the temperature (Schouten et al., 2006) or nutrient supply (Sachs and Kawka, 2015). Instead, we observed a nearly zero growth rate effect on expression of $^{2}\epsilon_{L/W}$ in *N. maritimus* despite using a 3-fold range of doubling time that is believed to encompass most of the natural conditions of marine AOA (e.g., (Qin et al., 2014; Santoro and Casciotti, 2011)). The direction of this response is the same as for haptophyte algae, with a decrease in $^{2}\epsilon_{L/W}$ (i.e., greater fractionation) observed at faster growth rates, but with a magnitude significantly less than what was observed for lipids of algae grown in chemostats (Sachs and Kawka, 2015). Previous work on *Haloarcula marismortui* (a halophilic archaea) showed variations in $^{2}\epsilon_{L/W}$ values up to 25‰ between fastest and slowest

growth (T_D from 8 to 16 h; (Dirghangi and Pagani, 2013). However, because the halophile work was done in batch culture, these doubling times reflect non-constant growth rates and integrate across the culture's growth stages, making direct comparison to our steady-state experiments difficult. We suggest that the highest growth-rate sensitivity for $^{2}\epsilon_{L/W}$ values of archaea likely would be expressed in cultures cultivated at maximum free energy (e.g., aerobically on simple sugars), and that studies in aerobic heterotrophs are necessary to confirm this end-member. Environmental conditions likely would be more constrained, and accordingly there should be less growth-rate variability in $^{2}\epsilon_{L/W}$ for natural archaeal communities, and especially for those that are autotrophic like the ammonia-oxidizing archaea.

Collectively our data support the idea that a unifying feature of the archaea is the operation of maximally energy-efficient metabolisms (Valentine, 2007). This is reflected by highly fractionated lipid δ^2H values, which are consistent with an overall metabolic status of having just enough NADPH or other internal electron donor to meet cellular demand (Wijker et al., 2019). We would further suggest that the inability to shift $^{2}\epsilon_{L/W}$ values off this minimum in *N. maritimus*, even when supplying electron donor at a high rate, indicates the marine Nitrososphaerota have inherently stable internal fluxes that were selected for during their adaptation to extreme oligotrophy (Martens-Habbena et al., 2009). This would be consistent with supply-side control of the rate of archaeal metabolism (Amenabar et al., 2017). Unless growth temperature has a significant impact, marine and lacustrine autotrophic Nitrososphaerota will have reliably invariant $^2H/^1H$ fractionation regardless of growth rate, nutrient status, or differences in community composition, and the environmental expression of archaeal $^{2}\epsilon_{L/W}$ may be more constant than for marine algae.

5.2.2. Distinguishing iGDGT sources using stable isotope patterns of biphytanes

Combining carbon and hydrogen isotope analyses of sedimentary biphytanes provides a powerful new means to disentangle sources and processes. In marine systems, compound distributions and carbon isotopic measurements indicate sedimentary iGDGTs appear to be derived mostly from local planktonic sources (Pearson et al., 2016; Shah et al., 2008; Zhang et al., 2016). Easily detectable exceptions are cases where methane cycling has affected the $\delta^{13}C$ ratios and iGDGT profiles of the sedimentary lipid pool (e.g., (Hoffmann-Sell et al., 2011; Sinninghe Damsté et al., 2001; Wakeham et al., 2003; Zhang et al., 2011). However, the resolution of $\delta^{13}C$ isotope ratio mass balance estimates is relatively coarse, and radiocarbon measurements can be logistically difficult to acquire in sufficient numbers to yield definitive conclusions. There are many instances of minor deviations in Ring Index (Zhang et al., 2016) or small but consistent differences between $\delta^{13}C$ values of iGDGTs – particularly the notable ^{13}C offset of ca. 1‰ between iGDGT-0 and crenarchaeol that occurs in many marine sediments (Elling et al., 2019; Pearson et al., 2016; Polik et al., 2018) – that require better understanding. Whether these signals are simply noise (e.g., due to sediment mixing or other factors), or whether they reflect systematic differences in sedimentary sources, is critical to the interpretation of iGDGT proxies such as the widely applied TEX_{86} sea-surface temperature proxy (Schouten et al., 2002). Such signals may be diagnosable through δ^2H analysis of individual BPs.

The iGDGTs in marine and lacustrine sediments therefore have the potential to integrate multiple sources, such that even if the dominant source is export of planktonic AOA, there also may be cases of significant input of benthic, soil-derived, or other allochthonous lipids. The distinctive pattern in relative $^{2}\epsilon_{L/W}$ values between BP chains of a single source could serve as an isotopic fingerprint to identify the contribution of these multiple iGDGT sources to sedimentary archives. BPs obtained from any sediment in which the archaeal lipids reflect a homogeneous community growing in a common body of water should have equal $\delta^{13}C$ values (Hurley et al., 2016), as well as predictable differences in δ^2H values that conform to the pattern BP-0 < BP-1 < BP-2 < BP-3. Of these,

the unique cyclohexane-containing BP-3 from crenarchaeol would serve as the anchor point for the planktonic signal.

A further advantage of this dual-stable isotope approach is the ability to obtain both sets of measurements (plus the overall iGDGT profile and the TEX_{86} ratio) from the same sample. This subverts the challenges of other multi-proxy approaches that may require comparison of lipid extracts to solid phases (e.g., elemental analyses for soil Al/Ti). Archaeal lipids from terrestrial freshwater environments are likely to be more depleted in 2H than those produced in seawater, with a differential that increases with latitude. Similarly, $\delta^{13}C$ values of archaeal BPs from continental sources may be either more negative or more variable than marine waters (Lattaud et al., 2021; Weijers et al., 2009). Dual C and H isotope patterns for BPs may prove particularly useful to diagnose terrestrial iGDGT inputs to marine sediments, thereby adding to the distribution metrics such as Ring Index, Methane Index, iGDGT-2/3 ratio, and other profiling strategies (Dunkley Jones et al., 2020; Taylor et al., 2013; Zhang et al., 2016, 2011) that currently are used to assess fidelity of the TEX_{86} index. Furthermore, the archaeal lipid-H proxy may be useful in tracking past climate through events such as the PETM in terrestrial records, and perhaps more recent shifts in the Plio-Pleistocene and Holocene.

5.3. Summary

In this study we quantified the hydrogen isotope fractionation between growth water and lipids in a well-studied strain of the ubiquitous marine ammonium oxidizing archaea in response to different steady-state electron donor fluxes. We observed little sensitivity to growth rate and a consistent pattern in the ordering of isotope fractionation with biphytane ring number. These observations are captured well in a bio-isotopic model, despite limited literature available on the intracellular hydride and electron carriers in environmentally important archaea. The results reveal that chemoautotrophic archaea such as *N. maritimus* add strongly 2H -depleted hydrogen during the saturation of isoprenoid chains of GDGTs, consistent with the values and patterns previously observed for phytol. Moreover, *N. maritimus* appears to be metabolically inflexible and may operate at large, constant NADPH deficit. Our data support the assertions of Wijker et al. (2019) that lipid $^{2}\epsilon_{L/W}$ patterns are governed by a set of universal KIEs in tandem with varying intracellular NADPH budgets. Further experimental work within the archaea, both in aerobic chemolithotrophs such as the AOAs, as well as in anaerobic chemolithotrophs and aerobic and anaerobic heterotrophs, will determine how useful archaeal lipid hydrogen isotopes will be for use in paleohydrology and paleoecology.

Declaration of Competing Interest

The authors declare that they have no known competing financial interests or personal relationships that could have appeared to influence the work reported in this paper.

Acknowledgments

This research was supported by funding from: collaborative research grant NSF EAR #1928303 (WDL, SHK); the American Chemical Society PRF #57209-DNI2 (WDL, YW); Simons Foundation Award #623881 (WDL); Swiss National Science Foundation P2BSP2_168716 (YW); NSF OCE-1843285 and 1702262 (AP); Dartmouth College via start-up funds (WDL); the University of Colorado Boulder via start-up funds and a seed grant to SHK; the Deutsche Forschungsgemeinschaft grant EL 898/2-1 (FJE). The authors thank Martin Könneke for providing strain SCM1; Xiahong Feng for assistance with water H-isotope measurements; Andrew Masterson for $H_{2(g)}$ measurements; as well as the analytical contributions of the CU Boulder Earth Systems Stable Isotope Lab (CUBES-SIL) Core Facility (RRID:SCR_019300). We thank the Executive Editor Jeff Catalano, Associate Editor Shucheng Xie. We especially thank

the reviewers: Alex Sessions, Maggie Osburn, and a third anonymous reviewer, whose detailed and constructive feedback substantially improved this manuscript.

Data availability

Access to all data products and code for this manuscript are available at: https://github.com/Kopflab/2023_leavitt_et_al.

Appendix A. Supplementary material

These include Supplemental Figs. 1–4, Supplemental Tables 1–2, and associate references, which encapsulate: all biphytane H-isotope values (Fig. S1); IRMS Calibration (Fig. S2), H-Isotope absolute error estimates (Fig. S3), a schematic of the 3HP/4HP pathway (Fig. S4), the biphytane H fractions (Table S1), and potential NADP(H) Sources in *N. maritimum* (Table S2). Permanently available online at: <https://doi.org/10.6084/m9.figshare.22701430.v1>. Supplementary material to this article can be found online at <https://doi.org/10.1016/j.gca.2023.04.033>.

References

- Addlesee, H.A., Gibson, L.C., Jensen, P.E., Hunter, C.N., 1996. Cloning, sequencing and functional assignment of the chlorophyll biosynthesis gene, chlP, of *Synechocystis* sp. PCC 6803. *FEBS Lett.* 389, 126–130.
- Amenabar, M.J., Shock, E.L., Roden, E.E., Peters, J.W., Boyd, E.S., 2017. Microbial substrate preference dictated by energy demand rather than supply. *Nat. Geosci.* 10, 577–581.
- Bayer, B., Pelikan, C., Bittner, M.J., Reinthaler, T., Könneke, M., Herndl, G.J., Offre, P., 2019. Proteomic response of three marine ammonia-oxidizing archaea to hydrogen peroxide and their metabolic interactions with a heterotrophic alphaproteobacterium. *Msystems* 4, e00181–e00219.
- Bender, A.L.D., Suess, M., Chitwood, D.H., Bradley, A.S., 2016. Investigating genetic loci that encode plant-derived paleoclimate proxies. Presented at the AGU Fall Meeting Abstracts, pp. PP24B-03.
- Boyd, E.S., Pearson, A., Pi, Y., Li, W.-J., Zhang, Y.G., He, L., Zhang, C.L., Geesey, G.G., 2011. Temperature and pH controls on glycerol dibiphytanyl glycerol tetraether lipid composition in the hyperthermophilic crenarchaeon *Acidilobus sulfurireducens*. *Extremophiles* 15, 59–65.
- Boyd, E.S., Hamilton, T.L., Wang, J., He, L., Zhang, C.L., 2013. The Role of Tetraether Lipid Composition in the Adaptation of Thermophilic Archaea to Acidity. *Front. Microbiol.* 4.
- Boyd, E.S., Amenabar, M.J., Poudel, S., Templeton, A.S., 2020. Bioenergetic constraints on the origin of autotrophic metabolism. *Philos. Transact. A Math. Phys. Eng. Sci.* 378, 20190151.
- Bräsen, C., Esser, D., Rauch, B., Siebers, B., 2014. Carbohydrate metabolism in Archaea: current insights into unusual enzymes and pathways and their regulation. *Microbiol. Mol. Biol. Rev.* 78, 89–175.
- Buckel, W., Thauer, R.K., 2013. Energy conservation via electron bifurcating ferredoxin reduction and proton/Na⁺ translocating ferredoxin oxidation. *Biochim. Biophys. Acta BBA-Bioenerg.* 1827, 94–113.
- Buckel, W., Thauer, R.K., 2018. Flavin-based electron bifurcation, ferredoxin, flavodoxin, and anaerobic respiration with protons (Ech) or NAD⁺ (Rnf) as electron acceptors: A historical review. *Front. Microbiol.* 9, 401.
- Campbell, B.J., Li, C., Sessions, A.L., Valentine, D.L., 2009. Hydrogen isotopic fractionation in lipid biosynthesis by H₂-consuming *Desulfobacterium autotrophicum*. *Geochim. Cosmochim. Acta* 73, 2744–2757.
- Campbell, B.J., Sessions, A.L., Fox, D.N., Paul, B.G., Qin, Q., Kellermann, M.Y., Valentine, D.L., 2017. Minimal influence of [NiFe] hydrogenase on hydrogen isotope fractionation in H₂-oxidizing *Cupriavidus necator*. *Front. Microbiol.* 8, 1886.
- Cha, Y., Murray, C.J., Klinman, J.P., 1989. Hydrogen tunneling in enzyme reactions. *Science* 243, 1325–1330.
- Chen, A., Dale Poulter, C., Kroon, P.A., 1994. Isoprenyl diphosphate synthases: protein sequence comparisons, a phylogenetic tree, and predictions of secondary structure. *Protein Sci.* 3, 600–607.
- Chen, A., Poulter, C., 1993. Purification and characterization of farnesyl diphosphate/geranylgeranyl diphosphate synthase. A thermostable bifunctional enzyme from *Methanobacterium thermoautotrophicum*. *J. Biol. Chem.* 268, 11002–11007.
- Chikaraishi, Y., Tanaka, R., Tanaka, A., Ohkouchi, N., 2009. Fractionation of hydrogen isotopes during phytol biosynthesis. *Org. Geochem.* 40, 569–573.
- Cobban, A., Zhang, Y., Zhou, A., Weber, Y., Elling, F.J., Pearson, A., Leavitt, W.D., 2020. Multiple environmental parameters impact lipid cyclization in *Sulfolobus acidocaldarius*. *Environ. Microbiol.* 22, 4046–4056.
- Damsté, J.S.S., Schouten, S., Hopmans, E.C., van Duin, A.C.T., Geenevasen, J.A.J., 2002. Crenarchaeol. *J. Lipid Res.* 43, 1641–1651.
- Dawson, D., Grice, K., Wang, S.X., Alexander, R., Radke, J., 2004. Stable hydrogen isotopic composition of hydrocarbons in torbanites (Late Carboniferous to Late Permian) deposited under various climatic conditions. *Org. Geochem.* 35, 189–197.
- Dawson, K.S., Osburn, M.R., Sessions, A.L., Orphan, V.J., 2015. Metabolic associations with archaea drive shifts in hydrogen isotope fractionation in sulfate-reducing bacterial lipids in cocultures and methane seeps. *Geobiology* 13, 462–477.
- De Rosa, M., Gambacorta, A., 1988. The lipids of archaeobacteria. *Prog. Lipid Res.* 27, 153–175.
- Dirghangi, S.S., Pagani, M., 2013. Hydrogen isotope fractionation during lipid biosynthesis by *Haloarcula marismortui*. *Geochim. Cosmochim. Acta* 119, 381–390.
- Dunkley Jones, T., Eley, Y.L., Thomson, W., Greene, S.E., Mandel, I., Edgar, K., Bendle, J. A., 2020. OPTIMAL: a new machine learning approach for GDGT-based palaeothermometry. *Clim. Past* 16, 2599–2617.
- Eiler, J.M., 2011. Paleoclimate reconstruction using carbonate clumped isotope thermometry. *Quat. Sci. Rev.* 30, 3575–3588.
- Elling, F.J., Könneke, M., Mußmann, M., Greve, A., Hinrichs, K.U., 2015. Influence of temperature, pH, and salinity on membrane lipid composition and TEX₈₆ of marine planktonic thaumarchaeal isolates. *Geochim. Cosmochim. Acta* 171, 238–255.
- Elling, F.J., Könneke, M., Nicol, G.W., Stieglmeier, M., Bayer, B., Spieck, E., de la Torre, J.R., Becker, K.W., Thomm, M., Prosser, J.I., 2017. Chemotaxonomic characterisation of the thaumarchaeal lipidome. *Environ. Microbiol.* 19, 2681–2700.
- Elling, F.J., Gottschalk, J., Doeana, K.D., Kusch, S., Hurley, S.J., Pearson, A., 2019. Archaeal lipid biomarker constraints on the Paleocene-Eocene carbon isotope excursion. *Nat. Commun.* 10, 1–10.
- Epstein, S., Buchsbaum, R., Lowenstam, H., Urey, H.C., 1951. Carbonate-water isotopic temperature scale. *Geol. Soc. Am. Bull.* 62, 417–426.
- Estep, M.F., Hoering, T.C., 1980. Biogeochemistry of the stable hydrogen isotopes. *Geochim. Cosmochim. Acta* 44, 1197–1206.
- Feyhl-Buska, J., Chen, Y., Jia, C., Wang, J.-X., Zhang, C.L., Boyd, E.S., 2016. Influence of growth phase, pH, and temperature on the abundance and composition of tetraether lipids in the Thermoacidophile *Picrophilus torridus*. *Front. Microbiol.* 7, 1323.
- Fuhrer, T., Sauer, U., 2009. Different biochemical mechanisms ensure network-wide balancing of reducing equivalents in microbial metabolism. *J. Bacteriol.* 191, 2112–2121.
- Gao, L., Hou, J., Toney, J., MacDonald, D., Huang, Y., 2011. Mathematical modeling of the aquatic macrophyte inputs of mid-chain n-alkyl lipids to lake sediments: Implications for interpreting compound specific hydrogen isotopic records. *Geochim. Cosmochim. Acta* 75, 3781–3791.
- Gat, J.R., 1996. Oxygen and hydrogen isotopes in the hydrologic cycle. *Annu. Rev. Earth Planet. Sci.* 24, 225–262.
- Hayakawa, H., Motoyama, K., Sobue, F., Ito, T., Kawaide, H., Yoshimura, T., Hemmi, H., 2018. Modified mevalonate pathway of the archaeon *Aeropyrum pernix* proceeds via trans-anhydromevalonate 5-phosphate. *Proc. Natl. Acad. Sci.* 115, 10034–10039.
- Hayes, J., 2001. Fractionation of the isotopes of carbon and hydrogen in biosynthetic processes. *Stable Isot. Geochem.* 43, 225–277.
- Heinzelmann, S.M., Villanueva, L., Sinke-Schoen, D., Sinnighe Damsté, J.S., Schouten, S., Van der Meer, M.T., 2015. Impact of metabolism and growth phase on the hydrogen isotope composition of microbial fatty acids. *Front. Microbiol.* 6, 408.
- Heinzelmann, S.M., Villanueva, L., Lipssew, Y.A., Sinke-Schoen, D., Damsté, J.S.S., Schouten, S., van der Meer, M.T., 2018. Assessing the metabolism of sedimentary microbial communities using the hydrogen isotopic composition of fatty acids. *Org. Geochem.* 124, 123–132.
- Hoffmann-Sell, L., Birgel, D., Arning, E.T., Föllmi, K.B., Peckmann, J., 2011. Archaeal lipids in Neogene dolomites (Monterey and Sisquoc Formations, California)—Planktic versus benthic archaeal sources. *Org. Geochem.* 42, 593–604.
- Hou, J., D'Andrea, W.J., Huang, Y., 2008. Can sedimentary leaf waxes record D/H ratios of continental precipitation? Field, model, and experimental assessments. *Geochim. Cosmochim. Acta* 72, 3503–3517.
- Hurley, S.J., Elling, F.J., Könneke, M., Buchwald, C., Wankel, S.D., Santoro, A.E., Lipp, J. S., Hinrichs, K.-U., Pearson, A., 2016. Influence of ammonia oxidation rate on thaumarchaeal lipid composition and the TEX₈₆ temperature proxy. *Proc. Natl. Acad. Sci.* 113, 7762–7767.
- Isobe, K., Ogawa, T., Hirose, K., Yokoi, T., Yoshimura, T., Hemmi, H., 2014. Geranylgeranyl Reductase and Ferredoxin from *Methanosarcina acetivorans* Are Required for the Synthesis of Fully Reduced Archaeal Membrane Lipid in *Escherichia coli* Cells. *J. Bacteriol.* 196, 417–423.
- Jackson, J.B., Peake, S.J., White, S.A., 1999. Structure and mechanism of proton-translocating transhydrogenase. *FEBS Lett.* 464, 1–8.
- Jain, S., Caforio, A., Driessen, A.J., 2014. Biosynthesis of archaeal membrane ether lipids. *Front. Microbiol.* 5, 641.
- Kahmen, A., Dawson, T.E., Vieth, A., Sachse, D., 2011. Leaf wax n-alkane δD values are determined early in the ontogeny of *Populus trichocarpa* leaves when grown under controlled environmental conditions. *Plant Cell Environ.* 34, 1639–1651.
- Kaneko, M., Kitajima, F., Naraoka, H., 2011. Stable hydrogen isotope measurement of archaeal ether-bound hydrocarbons. *Org. Geochem.* 42, 166–172.
- Keller, Y., Bouvier, F., d'Harlingue, A., Camara, B., 1998. Metabolic compartmentation of plastid prennylipid biosynthesis: evidence for the involvement of a multifunctional geranylgeranyl reductase. *Eur. J. Biochem.* 251, 413–417.
- Kellermann, M.Y., Yoshinaga, M.Y., Wegener, G., Krukenberg, V., Hinrichs, K.-U., 2016. Tracing the production and fate of individual archaeal intact polar lipids using stable isotope probing. *Org. Geochem.* 95, 13–20.
- Kim, J.-G., Park, S.-J., Damsté, J.S.S., Schouten, S., Rijpstra, W.I.C., Jung, M.-Y., Kim, S.-J., Gwak, J.-H., Hong, H., Si, O.-J., 2016. Hydrogen peroxide detoxification is a key mechanism for growth of ammonia-oxidizing archaea. *Proc. Natl. Acad. Sci.* 113, 7888–7893.
- Kim, J.-H., Schouten, S., Hopmans, E.C., Donner, B., Damsté, J.S.S., 2008. Global sediment core-top calibration of the TEX₈₆ paleothermometer in the ocean. *Geochim. Cosmochim. Acta* 72, 1154–1173.

- Kim, J.-H., Van der Meer, J., Schouten, S., Helmke, P., Willmott, V., Sangiorgi, F., Koç, N., Hopmans, E.C., Damsté, J.S.S., 2010. New indices and calibrations derived from the distribution of crenarchaeal isoprenoid tetraether lipids: Implications for past sea surface temperature reconstructions. *Geochim. Cosmochim. Acta* 74, 4639–4654.
- Koga, Y., Morii, H., 2007. Biosynthesis of ether-type polar lipids in archaea and evolutionary considerations. *Microbiol. Mol. Biol. Rev.* 71, 97–120.
- Könneke, M., Bernhard, A.E., José, R., Walker, C.B., Waterbury, J.B., Stahl, D.A., 2005. Isolation of an autotrophic ammonia-oxidizing marine archaeon. *Nature* 437, 543–546.
- Könneke, M., Schubert, D.M., Brown, P.C., Hügl, M., Standfest, S., Schwander, T., von Borzyskowski, L.S., Erb, T.J., Stahl, D.A., Berg, I.A., 2014. Ammonia-oxidizing archaea use the most energy-efficient aerobic pathway for CO₂ fixation. *Proc. Natl. Acad. Sci.* 111, 8239–8244.
- Köpf, S., Davidheiser-Kroll, B., Kocken, I., 2021. Isoreader: An R package to read stable isotope data files for reproducible research. *J. Open Source Softw.* 6, 2878.
- Köpf, S.H., McGlynn, S.E., Green-Saxena, A., Guan, Y., Newman, D.K., Orphan, V.J., 2015. Heavy water and 15 N labelling with N ano SIMS analysis reveals growth rate-dependent metabolic heterogeneity in chemostats. *Environ. Microbiol.* 17, 2542–2556.
- Köpf, S.H., 2015. From lakes to lungs: Assessing microbial activity in diverse environments.
- Kreuzer-Martin, H.W., Lott, M.J., Ehleringer, J.R., Hegg, E.L., 2006. Metabolic processes account for the majority of the intracellular water in log-phase *Escherichia coli* cells as revealed by hydrogen isotopes. *Biochemistry* 45, 13622–13630.
- Lattaud, J., De Jonge, C., Pearson, A., Elling, F.J., Eglinton, T.I., 2021. Microbial lipid signatures in Arctic deltaic sediments—Insights into methane cycling and climate variability. *Org. Geochem.* 157, 104242.
- Leavitt, W.D., Flynn, T.M., Suess, M.K., Bradley, A.S., 2016a. Transhydrogenase and Growth Substrate Influence Lipid Hydrogen Isotope Ratios in *Desulfovibrio alaskensis* G20. *Front. Microbiol.* 07, 918.
- Leavitt, W.D., Venceslau, S.S., Pereira, I.A., Johnston, D.T., Bradley, A.S., 2016b. Fractionation of sulfur and hydrogen isotopes in *Desulfovibrio vulgaris* with perturbed DsrC expression. *FEMS Microbiol. Lett.* 363, ffw226.
- Leavitt, W.D., Murphy, S.-J.-L., Lynd, L.R., Bradley, A.S., 2017. Hydrogen isotope composition of *Thermoanaerobacterium saccharolyticum* lipids: Comparing wild type with a *nfn*-transhydrogenase mutant. *Org. Geochem.* 113, 239–241.
- Leavitt, W.D., Venceslau, S.S., Waldbauer, J., Smith, D.A., Pereira, I.A.C., Bradley, A.S., 2019. Proteomic and isotopic response of *Desulfovibrio vulgaris* to DsrC perturbation. *Front. Microbiol.* 10, 658.
- Lengger, S.K., Weber, Y., Taylor, K.W., Köpf, S.H., Berstan, R., Bull, I.D., Maysers, J., Leavitt, W.D., Blewett, J., Pearson, A., 2021. Determination of the $\delta^2\text{H}$ values of high molecular weight lipids by high-temperature gas chromatography coupled to isotope ratio mass spectrometry. *Rapid Commun. Mass Spectrom.* 35, e8983.
- Li, C., Sessions, A.L., Kinnaman, F.S., Valentine, D.L., 2009. Hydrogen-isotopic variability in lipids from Santa Barbara Basin sediments. *Geochim. Cosmochim. Acta* 73, 4803–4823.
- Lloyd, C.T., Iwig, D.F., Wang, B., Cossu, M., Metcalf, W.W., Boal, A.K., Booker, S.J., 2022. Discovery, structure and mechanism of a tetraether lipid synthase. *Nature* 609, 197–203.
- Maloney, A.E., Shinneman, A.L., Hemeon, K., Sachs, J.P., 2016. Exploring lipid $^2\text{H}/^1\text{H}$ fractionation mechanisms in response to salinity with continuous cultures of the diatom *Thalassiosira pseudonana*. *Org. Geochem.* 101, 154–165.
- Martens-Habbena, W., Berube, P.M., Urakawa, H., José, R., Stahl, D.A., 2009. Ammonia oxidation kinetics determine niche separation of nitrifying Archaea and Bacteria. *Nature* 461, 976–979.
- McCrea, J.M., 1950. On the isotopic chemistry of carbonates and a paleotemperature scale. *J. Chem. Phys.* 18, 849–857.
- McFarlin, J.M., Axford, Y., Masterson, A.L., Osburn, M.R., 2019. Calibration of modern sedimentary $\delta^2\text{H}$ plant wax-water relationships in Greenland lakes. *Quat. Sci. Rev.* 225, 105978.
- McInerney, F.A., Helliker, B.R., Freeman, K.H., 2011. Hydrogen isotope ratios of leaf wax n-alkanes in grasses are insensitive to transpiration. *Geochim. Cosmochim. Acta* 75, 541–554.
- Murakami, M., Shibuya, K., Nakayama, T., Nishino, T., Yoshimura, T., Hemmi, H., 2007. Geranylgeranyl reductase involved in the biosynthesis of archaeal membrane lipids in the hyperthermophilic archaeon *Archaeoglobus fulgidus*. *FEBS J.* 274, 805–814.
- Nagel, Z.D., Klinman, J.P., 2006. Tunneling and dynamics in enzymatic hydride transfer. *Chem. Rev.* 106, 3095–3118.
- Nishimura, Y., Eguchi, T., 2006. Biosynthesis of archaeal membrane lipids: digeranylgeranylgerolphospholipid reductase of the thermoacidophilic archaeon *Thermoplasma acidophilum*. *J. Biochem.* 139, 1073–1081.
- Nunn, C.E., Johnsen, U., Schönheit, P., Fuhrer, T., Sauer, U., Hough, D.W., Danson, M.J., 2010. Metabolism of pentose sugars in the hyperthermophilic archaea *Sulfolobus solfataricus* and *Sulfolobus acidocaldarius*. *J. Biol. Chem.* 285, 33701–33709.
- Oger, P.M., Cario, A., 2013. Adaptation of the membrane in Archaea. *Biophys. Chem.* 183, 42–56.
- Osburn, M.R., Dawson, K.S., Fogel, M.L., Sessions, A.L., 2016. Fractionation of hydrogen isotopes by sulfate- and nitrate-reducing bacteria. *Front. Microbiol.* 7, 1166.
- Pearson, A., 2019. Resolving a piece of the archaeal lipid puzzle. *Proc. Natl. Acad. Sci.* 116, 22423–22425.
- Pearson, A., Hurley, S.J., Walter, S.R.S., Kusch, S., Lichtin, S., Zhang, Y.G., 2016. Stable carbon isotope ratios of intact GDGTs indicate heterogeneous sources to marine sediments. *Geochim. Cosmochim. Acta* 181, 18–35.
- Pearson, A., Ingalls, A.E., 2013. Assessing the use of archaeal lipids as marine environmental proxies. *Annu. Rev. Earth Planet. Sci.* 41, 359–384.
- Polik, C.A., Elling, F.J., Pearson, A., 2018. Impacts of paleoecology on the TEX86 sea surface temperature proxy in the Pliocene-Pleistocene Mediterranean Sea. *Paleoceanogr. Paleoclimatology* 33, 1472–1489.
- Poudel, S., Dunham, E.C., Lindsay, M.R., Amenabar, M.J., Fones, E.M., Colman, D.R., Boyd, E.S., 2018. Origin and evolution of flavin-based electron bifurcating enzymes. *Front. Microbiol.* 9, 1762.
- Powers, L., Werne, J.P., Vanderwoude, A.J., Damsté, J.S.S., Hopmans, E.C., Schouten, S., 2010. Applicability and calibration of the TEX86 paleothermometer in lakes. *Org. Geochem.* 41, 404–413.
- Pudney, C.R., Hay, S., Levy, C., Pang, J., Sutcliffe, M.J., Leys, D., Scrutton, N.S., 2009a. Evidence to support the hypothesis that promoting vibrations enhance the rate of an enzyme catalyzed H-tunneling reaction. *J. Am. Chem. Soc.* 131, 17072–17073.
- Pudney, C.R., Hay, S., Scrutton, N.S., 2009b. Bipartite recognition and conformational sampling mechanisms for hydride transfer from nicotinamide coenzyme to FMN in pentaerythritol tetranitrate reductase. *FEBS J.* 276, 4780–4789.
- Qin, W., Amin, S.A., Martens-Habbena, W., Walker, C.B., Urakawa, H., Devol, A.H., Ingalls, A.E., Moffett, J.W., Armbrust, E.V., Stahl, D.A., 2014. Marine ammonia-oxidizing archaeal isolates display obligate mixotrophy and wide ecotypic variation. *Proc. Natl. Acad. Sci.* 111, 12504–12509.
- Quehenberger, J., Pittenauer, E., Allmaier, G., Spadiut, O., 2020. The influence of the specific growth rate on the lipid composition of *Sulfolobus acidocaldarius*. *Extremophiles* 24, 413.
- Ren, M., Feng, X., Huang, Y., Wang, H., Hu, Z., Clingenpeel, S., Swan, B.K., Fonseca, M. M., Posada, D., Stepanauskas, R., Hollibaugh, J.T., Foster, P.G., Woyke, T., Luo, H., 2019. Phylogenomics suggests oxygen availability as a driving force in Thaumarchaeota evolution. *ISME J.* 13, 2150–2161.
- Robert, F., 2001. The Origin of Water on Earth. *Science* 293, 1056.
- Sachs, J.P., 2014. Hydrogen Isotope Signatures in the Lipids of Phytoplankton. In: *Treatise on Geochemistry*. Elsevier, pp. 79–94.
- Sachs, J.P., Kawka, O.E., 2015. The influence of growth rate on $^2\text{H}/^1\text{H}$ fractionation in continuous cultures of the coccolithophorid *Emiliania huxleyi* and the diatom *Thalassiosira pseudonana*. *Plos One* 10, e0141643.
- Sachs, J.P., Maloney, A.E., Gregersen, J., Paschall, C., 2016. Effect of salinity on $^2\text{H}/^1\text{H}$ fractionation in lipids from continuous cultures of the coccolithophorid *Emiliania huxleyi*. *Geochim. Cosmochim. Acta* 189, 96–109.
- Sachs, J.P., Maloney, A.E., Gregersen, J., 2017. Effect of light on $^2\text{H}/^1\text{H}$ fractionation in lipids from continuous cultures of the diatom *Thalassiosira pseudonana*. *Geochim. Cosmochim. Acta* 209, 204–215.
- Sachse, D., Gleixner, G., Wilkes, H., Kahmen, A., 2010. Leaf wax n-alkane δD values of field-grown barley reflect leaf water δD values at the time of leaf formation. *Geochim. Cosmochim. Acta* 74, 6741–6750.
- Sachse, D., Billault, I., Bowen, G.J., Chikaraishi, Y., Dawson, T.E., Feakins, S.J., Freeman, K.H., Magill, C.R., McInerney, F.A., Van Der Meer, M.T., 2012. Molecular paleohydrology: interpreting the hydrogen-isotopic composition of lipid biomarkers from photosynthesizing organisms. *Annu. Rev. Earth Planet. Sci.* 40, 221–249.
- Santoro, A.E., Casciotti, K.L., 2011. Enrichment and characterization of ammonia-oxidizing archaea from the open ocean: phylogeny, physiology and stable isotope fractionation. *ISME J.* 5, 1796–1808.
- Sasaki, D., Fujihashi, M., Iwata, Y., Murakami, M., Yoshimura, T., Hemmi, H., Miki, K., 2011. Structure and Mutation Analysis of Archaeal Geranylgeranyl Reductase. *J. Mol. Biol.* 409, 543–557.
- Sato, S., Murakami, M., Yoshimura, T., Hemmi, H., 2008. Specific Partial Reduction of Geranylgeranyl Diphosphate by an Enzyme from the Thermoacidophilic Archaeon *Sulfolobus acidocaldarius* Yields a Reactive Prenyl Donor, Not a Dead-End Product. *J. Bacteriol.* 190, 3923–3929.
- Sauer, U., Canonaco, F., Heri, S., Perrenoud, A., Fischer, E., 2004. The soluble and membrane-bound transhydrogenases UdhA and PntAB have divergent functions in NADPH metabolism of *Escherichia coli*. *J. Biol. Chem.* 279, 6613–6619.
- Schimmelmann, A., Sessions, A.L., Mastalerz, M., 2006. Hydrogen isotopic (D/H) composition of organic matter during diagenesis and thermal maturation. *Annu. Rev. Earth Planet. Sci.* 34, 501–533.
- Schouten, S., Hopmans, E.C., Schefuß, E., Damsté, J.S.S., 2002. Distributional variations in marine crenarchaeotal membrane lipids: a new tool for reconstructing ancient sea water temperatures? *Earth Planet. Sci. Lett.* 204, 265–274.
- Schouten, S., Ossebaar, J., Schreiber, K., Kienhuis, M., Langer, G., Benthien, A., Bijma, J., 2006. The effect of temperature, salinity and growth rate on the stable hydrogen isotopic composition of long chain alkenones produced by *Emiliania huxleyi* and *Gephyrocapsa oceanica*. *Biogeosciences* 3, 113–119.
- Schouten, S., Hopmans, E.C., Damsté, J.S.S., 2013. The organic geochemistry of glycerol dialkyl glycerol tetraether lipids: A review. *Org. Geochem.* 54, 19–61.
- Sessions, A.L., 2016. Factors controlling the deuterium contents of sedimentary hydrocarbons. *Org. Geochem.* 96, 43–64.
- Sessions, A.L., Burgoyne, T.W., Schimmelmann, A., Hayes, J.M., 1999. Fractionation of hydrogen isotopes in lipid biosynthesis. *Org. Geochem.* 30, 1193–1200.
- Sessions, A.L., Jahnke, L.L., Schimmelmann, A., Hayes, J.M., 2002. Hydrogen isotope fractionation in lipids of the methane-oxidizing bacterium *Methylococcus capsulatus*. *Geochim. Cosmochim. Acta* 66, 3955–3969.
- Sessions, A.L., Sylva, S.P., Summons, R.E., Hayes, J.M., 2004. Isotopic exchange of carbon-bound hydrogen over geologic timescales. *Geochim. Cosmochim. Acta* 68, 1545–1559.
- Shafiee, R.T., Snow, J.T., Hester, S., Zhang, Q., Rickaby, R.E., 2022. Proteomic response of the marine ammonia-oxidizing archaeon *Nitrosopumilus maritimus* to iron limitation reveals strategies to compensate for nutrient scarcity. *Environ. Microbiol.* 24, 835–849.

- Shah, S.R., Mollenhauer, G., Ohkouchi, N., Eglinton, T.I., Pearson, A., 2008. Origins of archaeal tetraether lipids in sediments: Insights from radiocarbon analysis. *Geochim. Cosmochim. Acta* 72, 4577–4594.
- Sinninghe Damsté, J., Pancost, R., Hopmans, E., 2001. Archaeal lipids in Mediterranean Cold Seeps: Molecular proxies for anaerobic methane oxidation. *Geochim. Cosmochim. Acta* 65, 1611.
- Sinninghe Damsté, J.S., Weber, Y., Zopfi, J., Lehmann, M.F., Niemann, H., 2022. Distributions and sources of isoprenoidal GDGTs in Lake Lugano and other central European (peri-)alpine lakes: Lessons for their use as paleotemperature proxies. *Quat. Sci. Rev.* 277, 107352.
- Smith, F.A., Freeman, K.H., 2006. Influence of physiology and climate on δD of leaf wax n-alkanes from C3 and C4 grasses. *Geochim. Cosmochim. Acta* 70, 1172–1187.
- Spaans, S.K., Weusthuis, R.A., Van Der Oost, J., Kengen, S.W., 2015. NADPH-generating systems in bacteria and archaea. *Front. Microbiol.* 6, 742.
- Taenzler, L., Labidi, J., Masterson, A.L., Feng, X., Rumble III, D., Young, E.D., Leavitt, W. D., 2020. Low $\Delta^{12}CH_2D_2$ values in microbialgenic methane result from combinatorial isotope effects. *Geochim. Cosmochim. Acta* 285, 225–236.
- Taylor, K.W., Huber, M., Hollis, C.J., Hernandez-Sanchez, M.T., Pancost, R.D., 2013. Re-evaluating modern and Palaeogene GDGT distributions: Implications for SST reconstructions. *Glob. Planet. Change* 108, 158–174.
- Tierney, J.E., Tingley, M.P., 2014. A Bayesian, spatially-varying calibration model for the TEX86 proxy. *Geochim. Cosmochim. Acta* 127, 83–106.
- Tierney, J.E., Tingley, M.P., 2015. A TEX86 surface sediment database and extended Bayesian calibration. *Sci. Data* 2, 1–10.
- Tipple, B.J., Berke, M.A., Doman, C.E., Khachatryan, S., Ehleringer, J.R., 2013. Leaf-wax n-alkanes record the plant–water environment at leaf flush. *Proc. Natl. Acad. Sci.* 110, 2659–2664.
- Tourte, M., Schaeffer, P., Grossi, V., Oger, P.M., 2022. Membrane adaptation in the hyperthermophilic archaeon *Pyrococcus furiosus* relies upon a novel strategy involving glycerol monoalkyl glycerol tetraether lipids. *Environ. Microbiol.* 24, 2029–2046.
- Valentine, D.L., 2007. Adaptations to energy stress dictate the ecology and evolution of the Archaea. *Nat. Rev. Microbiol.* 5, 316–323.
- Valentine, D., Sessions, A., Tyler, S., Chidthaisong, A., 2004. Hydrogen isotope fractionation during H_2/CO_2 acetogenesis: hydrogen utilization efficiency and the origin of lipid-bound hydrogen. *Geobiology* 2, 179–188.
- van der Meer, M.T., Benthien, A., French, K.L., Epping, E., Zondervan, I., Reichart, G.-J., Bijma, J., Damsté, J.S.S., Schouten, S., 2015. Large effect of irradiance on hydrogen isotope fractionation of alkenones in *Emiliania huxleyi*. *Geochim. Cosmochim. Acta* 160, 16–24.
- Wakeham, S.G., Lewis, C.M., Hopmans, E.C., Schouten, S., Damsté, J.S.S., 2003. Archaea mediate anaerobic oxidation of methane in deep euxinic waters of the Black Sea. *Geochim. Cosmochim. Acta* 67, 1359–1374.
- Walker, C.B., De La Torre, J., Klotz, M., Urakawa, H., Pinel, N., Arp, D., Brochier-Armanet, C., Chain, P., Chan, P., Gollabgir, A., 2010. *Nitrosopumilus maritimus* genome reveals unique mechanisms for nitrification and autotrophy in globally distributed marine crenarchaea. *Proc. Natl. Acad. Sci.* 107, 8818–8823.
- Wang, Y., Sessions, A.L., Nielsen, R.J., Goddard III, W.A., 2009. Equilibrium $^2H/^1H$ fractionations in organic molecules: I. Experimental calibration of ab initio calculations. *Geochim. Cosmochim. Acta* 73, 7060–7075.
- Wegener, G., Kellermann, M.Y., Elvert, M., 2016. Tracking activity and function of microorganisms by stable isotope probing of membrane lipids. *Anal. Biotechnol.* 41, 43–52.
- Weijers, J.W., Schouten, S., Schefuß, E., Schneider, R.R., Damsté, J.S.S., 2009. Disentangling marine, soil and plant organic carbon contributions to continental margin sediments: a multi-proxy approach in a 20,000 year sediment record from the Congo deep-sea fan. *Geochim. Cosmochim. Acta* 73, 119–132.
- Weiss, G.M., Pfannerstill, E.Y., Schouten, S., Sinninghe Damsté, J.S., van der Meer, M.T., 2017. Effects of alkalinity and salinity at low and high light intensity on hydrogen isotope fractionation of long-chain alkenones produced by *Emiliania huxleyi*. *Biogeosciences* 14, 5693–5704.
- Wijker, R.S., Sessions, A.L., Fuhrer, T., Phan, M., 2019. $^2H/^1H$ variation in microbial lipids is controlled by NADPH metabolism. *Proc. Natl. Acad. Sci.* 116, 12173–12182.
- Wolfshorndl, M., Danford, R., Sachs, J.P., 2019. $^2H/^1H$ fractionation in microalgal lipids from the North Pacific Ocean: Growth rate and irradiance effects. *Geochim. Cosmochim. Acta* 246, 317–338.
- Wu, W., Meador, T.B., Könneke, M., Elvert, M., Wegener, G., Hinrichs, K., 2020. Substrate-dependent incorporation of carbon and hydrogen for lipid biosynthesis by *Methanosarcina barkeri*. *Environ. Microbiol. Rep.* 12, 555–567.
- Yang, W., Chen, H., Chen, Y., Chen, A., Feng, X., Zhao, B., Zheng, F., Fang, H., Zhang, C., Zeng, Z., 2023. Thermophilic archaeon orchestrates temporal expression of GDGT ring syntheses in response to temperature and acidity stress. *Environ. Microbiol.* 25, 575–587.
- Zeng, Z., Liu, X.-L., Farley, K.R., Wei, J.H., Metcalf, W.W., Summons, R.E., Welander, P. V., 2019. GDGT cyclization proteins identify the dominant archaeal sources of tetraether lipids in the ocean. *Proc. Natl. Acad. Sci.* 201909306
- Zeng, Z., Chen, H., Yang, H., Chen, Y., Yang, W., Feng, X., Pei, H., Welander, P.V., 2022. Identification of a protein responsible for the synthesis of archaeal membrane-spanning GDGT lipids. *Nat. Commun.* 13, 1545.
- Zhang, X., Gillespie, A.L., Sessions, A.L., 2009. Large D/H variations in bacterial lipids reflect central metabolic pathways. *Proc. Natl. Acad. Sci.* 106, 12580–12586.
- Zhang, Y.G., Zhang, C.L., Liu, X.-L., Li, L., Hinrichs, K.-U., Noakes, J.E., 2011. Methane Index: A tetraether archaeal lipid biomarker indicator for detecting the instability of marine gas hydrates. *Earth Planet. Sci. Lett.* 307, 525–534.
- Zhang, Y.G., Pagani, M., Wang, Z., 2016. Ring Index: A new strategy to evaluate the integrity of TEX86 paleothermometry. *Paleoceanography* 31, 220–232.
- Zhou, A., Weber, Y., Chiu, B.K., Elling, F.J., Cobban, A.B., Pearson, A., Leavitt, W.D., 2020. Energy flux controls tetraether lipid cyclization in *Sulfolobus acidocaldarius*. *Environ. Microbiol.* 22, 343–353.

Controls on the hydrogen isotope composition of tetraether lipids in an autotrophic ammonia-oxidizing marine archaeon

W. D. Leavitt^{*,†,1,2}, S. H. Kopf^{§,†}, Y. Weber^{4,§}, B. Chiu^{1,‡}, J. M. McFarlin^{3,4}, F. J. Elling^{5,6}, S. Hoefft-McCann^{5,¶}, A. Pearson⁵

APPENDIX A:

Supplemental Figures 1: All Biphytane H-Isotope Data.

Supplemental Figures 2: IRMS Calibration .

Supplemental Figures 3: H-Isotope Absolute Error Estimates.

Supplemental Figures 4: 3HP/4HP Pathway.

Supplemental References

Supplemental Table 1: Biphytane H Fractions (Number of H)

Supplemental Table 2: Potential NADP(H) Sources in *N. maritimus*

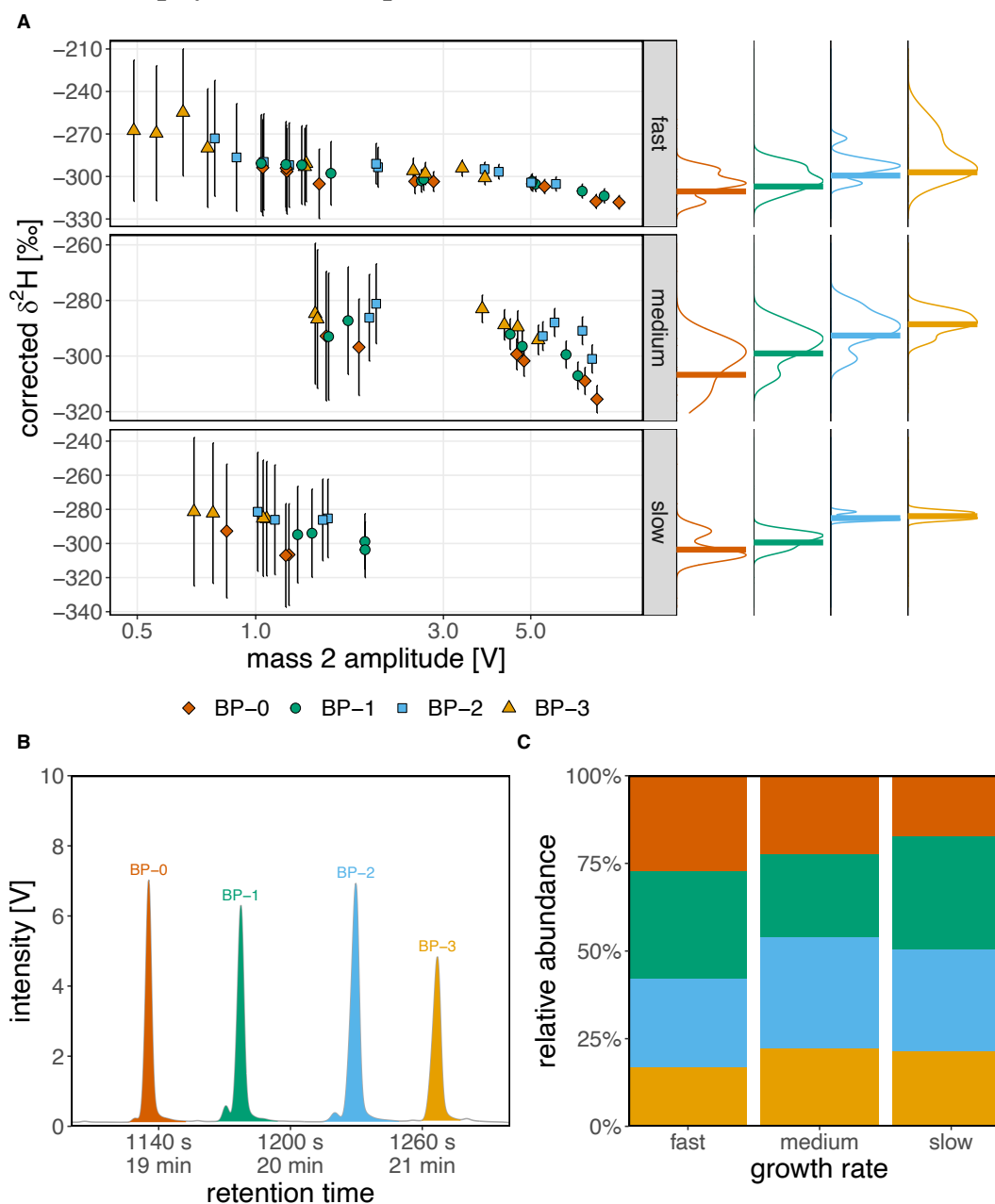
Figure S1: All Biphytane H-Isotope Data

Figure S1. (A) Replicate hydrogen isotope measurements of archaeal biphytanes (BPs) from *N. maritimus*. All isotope values are calibrated against the A6 alkane standard and corrected for alkyl iodide hydrogenation ($\delta^2\text{H}_{\text{cor}}$) with propagated errors (σ_{cor}) from hydrogenation and peak-size adjusted uncertainties as described in the methods section. **(B)** Example chromatogram showing mass-2 trace of GC-P-IRMS analysis with BPs highlighted. **(C)** Relative abundances of BPs at the “Fast”, “Medium”, and “Slow” growth rates used in this study (see Table 1 for doubling times).

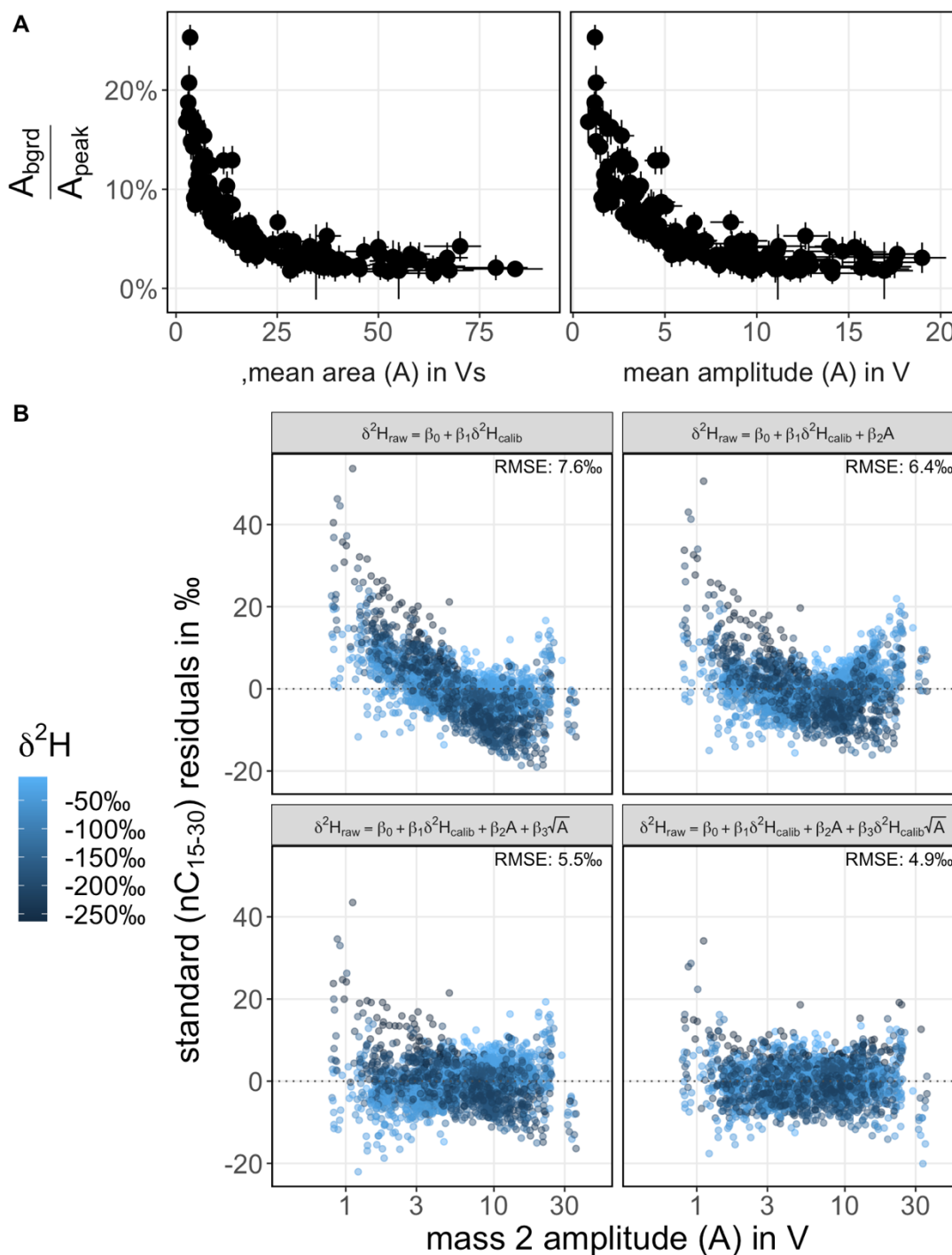
Figure S2: IRMS Calibration

Figure S2. (A). Theoretical background estimate from 144 individual linear regressions of A6 standard analyses ($\delta_{\text{peak}/\text{H}_2} = \beta_1 \cdot \delta_{\text{analyte}/\text{VSMOW}} + \beta_0$) suggesting a peak-size effect that can be parameterized vs. peak area or peak amplitude. Error bars in y are standard errors propagated from the linear regression coefficients as derived below. Error bars in x represent the range of peak areas/amplitudes for each standard analysis. The relative background estimates are derived from mass balance considerations of a theoretical background contribution to each analyte peak:

$$\begin{aligned}
R_{peak} &= \frac{A_{peak} - A_{bgrd}}{A_{peak}} R_{analyte} + \frac{A_{bgrd}}{A_{peak}} R_{bgrd} \\
\delta_{peak/H2} &= \frac{R_{peak}}{R_{H2}} - 1 \\
&= \left[\frac{A_{peak} - A_{bgrd}}{A_{peak}} \frac{R_{analyte}}{R_{VSMOW}} + \frac{A_{bgrd}}{A_{peak}} \frac{R_{bgrd}}{R_{VSMOW}} \right] \cdot \frac{R_{VSMOW}}{R_{H2}} - 1 \\
&= \left[\frac{A_{peak} - A_{bgrd}}{A_{peak}} (\delta_{analyte/VSMOW} + 1) + \frac{A_{bgrd}}{A_{peak}} (\delta_{bgrd/VSMOW} + 1) \right] \cdot \frac{R_{VSMOW}}{R_{H2}} - 1 \\
&= \frac{R_{VSMOW}}{R_{H2}} \delta_{analyte/VSMOW} - \frac{R_{VSMOW}}{R_{H2}} \frac{A_{bgrd}}{A_{peak}} \delta_{analyte/VSMOW} + \frac{R_{VSMOW}}{R_{H2}} \cdot \frac{A_{bgrd}}{A_{peak}} \delta_{bgrd/VSMOW} \\
&\quad + \frac{R_{VSMOW}}{R_{H2}} - 1
\end{aligned}$$

with the resulting univariate linear regression at approximately constant peak size for each individual standard analysis ($\delta_{peak/H2} = \beta_1 \cdot \delta_{analyte/VSMOW} + \beta_0$) constraining the regression coefficients (intercept and slope) as $\beta_0 = \frac{R_{VSMOW}}{R_{H2}} \frac{A_{bgrd}}{A_{peak}} \delta_{bgrd/VSMOW} + \frac{R_{VSMOW}}{R_{H2}} - 1$ and $\beta_1 = \frac{R_{VSMOW}}{R_{H2}} \left(1 - \frac{A_{bgrd}}{A_{peak}}\right)$ and allowing for the estimation of $\frac{A_{bgrd}}{A_{peak}} = \frac{1 + \beta_0 - \beta_1}{1 + \beta_0 + \delta_{bgrd} \cdot \beta_1} \approx 1 - \frac{\beta_1}{1 + \beta_0}$ from the regression coefficients as visualized in panel A:

$$\begin{aligned}
R_{peak} &= \frac{A_{peak} - A_{bgrd}}{A_{peak}} R_{analyte} + \frac{A_{bgrd}}{A_{peak}} R_{bgrd} \\
\delta_{peak/H2} &= \frac{R_{peak}}{R_{H2}} - 1 \\
&= \left[\frac{A_{peak} - A_{bgrd}}{A_{peak}} \frac{R_{analyte}}{R_{VSMOW}} + \frac{A_{bgrd}}{A_{peak}} \frac{R_{bgrd}}{R_{VSMOW}} \right] \cdot \frac{R_{VSMOW}}{R_{H2}} - 1 \\
&= \left[\frac{A_{peak} - A_{bgrd}}{A_{peak}} (\delta_{analyte/VSMOW} + 1) + \frac{A_{bgrd}}{A_{peak}} (\delta_{bgrd/VSMOW} + 1) \right] \cdot \frac{R_{VSMOW}}{R_{H2}} - 1 \\
&= \frac{R_{VSMOW}}{R_{H2}} \delta_{analyte/VSMOW} - \frac{R_{VSMOW}}{R_{H2}} \frac{A_{bgrd}}{A_{peak}} \delta_{analyte/VSMOW} + \frac{R_{VSMOW}}{R_{H2}} \cdot \frac{A_{bgrd}}{A_{peak}} \delta_{bgrd/VSMOW} \\
&\quad + \frac{R_{VSMOW}}{R_{H2}} - 1
\end{aligned}$$

with the resulting univariate linear regression at approximately constant peak size for each individual standard analysis ($\delta_{peak/H2} = \beta_1 \cdot \delta_{analyte/VSMOW} + \beta_0$) constraining the regression coefficients as $\beta_0 = \frac{R_{VSMOW}}{R_{H2}} \frac{A_{bgrd}}{A_{peak}} \delta_{bgrd/VSMOW} + \frac{R_{VSMOW}}{R_{H2}} - 1$ and $\beta_1 = \frac{R_{VSMOW}}{R_{H2}} \left(1 - \frac{A_{bgrd}}{A_{peak}}\right)$ and allowing for the estimation of $\frac{A_{bgrd}}{A_{peak}} = \frac{1 + \beta_0 - \beta_1}{1 + \beta_0 + \delta_{bgrd} \cdot \beta_1} \approx 1 - \frac{\beta_1}{1 + \beta_0}$ from the regression coefficients (assuming $|\delta_{bgrd}| \ll 1000\%$) as visualized in (A). To account for the peak-size effects, a multivariate linear regression with both isotopic composition and peak size terms is used across all standards to calibrate the sample data. **(B)** shows the resulting residuals of the 2195 compound-specific H isotope measurements from the A6 standard compounds (C₁₅ through C₃₀ *n*-alkanes) using 4 potential calibration models. The regression equation and root-mean-square error (RMSE) of each model are shown in their respective panel. The regression model whose residuals are shown in the lower right panel ($\delta^2H_{raw} = \beta_0 + \beta_1 \cdot \delta^2H_{cal} + \beta_2 \cdot A + \beta_3 \cdot \delta^2H_{cal} \cdot \sqrt{A}$, RMSE 4.9 ‰) is the one used for calibration as discussed in the main text. Raw data and processing scripts for GC-P-IRMS output are available at: https://github.com/KopfLab/2023_leavitt_et_al.

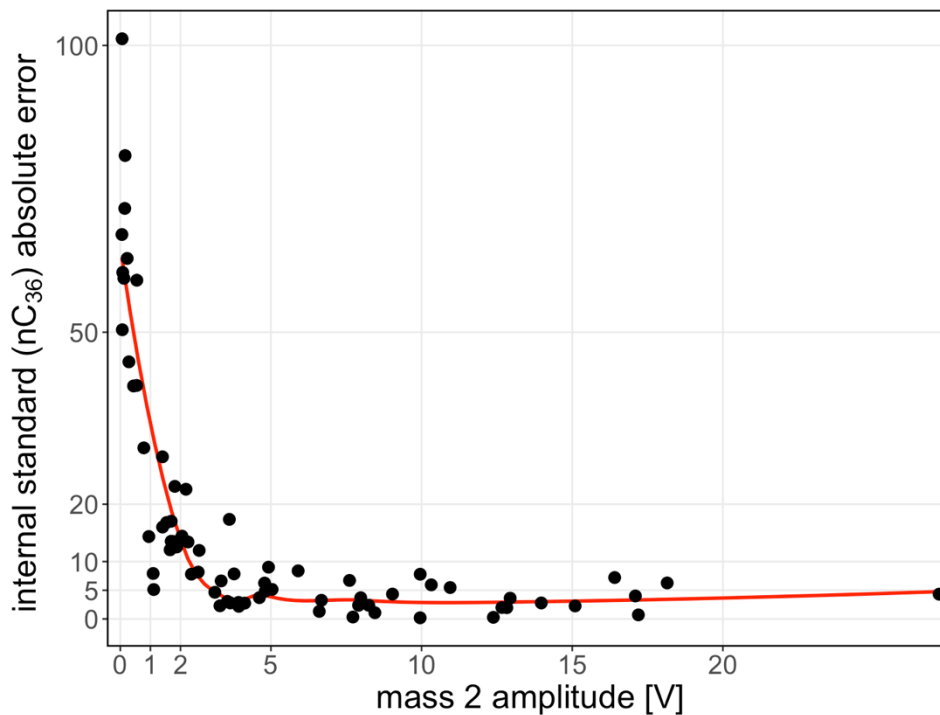
Figure S3: H-Isotope Absolute Error Estimates

Figure S3. Absolute error of the calibrated $\delta^2\text{H}_{\text{cal}}$ values of the nC₃₆ standard (n=73) vs its known isotopic composition. The red line represents a local polynomial regression fit and was used to determine peak-sized adjusted error estimates for the $\delta^2\text{H}_{\text{cal}}$ values (σ_{cal}) of the measured biphytanes (Figures 1 and S1).

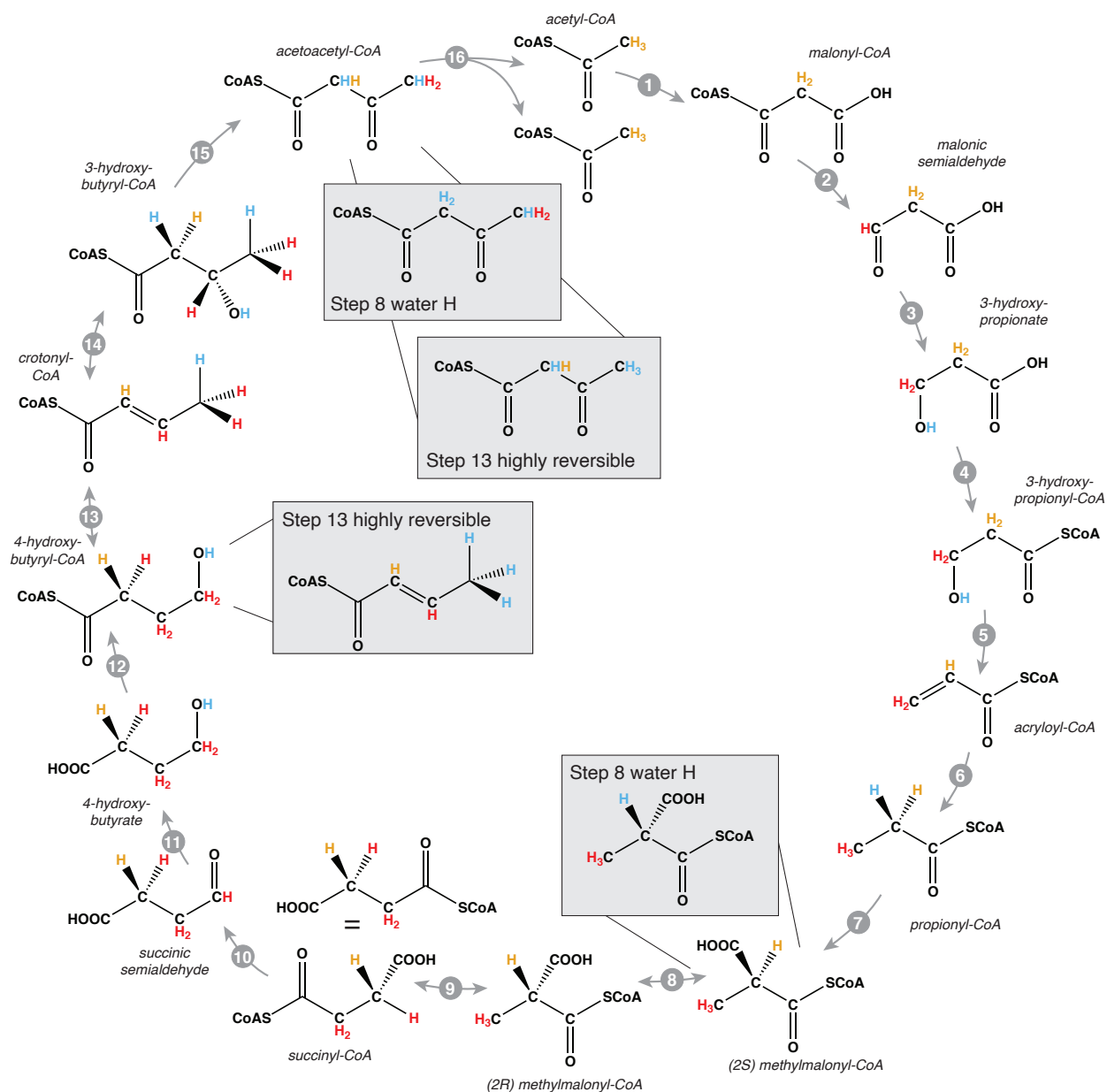
Figure S4: 3HP/4HP Pathway

Figure S4. Origin of the methyl group hydrogens of acetyl-CoA derived from the 3HP/4HP (3-hydroxypropionate / 4-hydroxybutyrate) cycle. The H from **water** (protons) are shown in **blue**; H from **NADPH** in **red**. One full turn of the cycle generates newly biosynthesized acetyl-CoA (**orange**) in which all H were originally derived from **water** and **NADPH**; all, or all but one, of these H are replaced by the next turn of the cycle. The color coding shows H sources for the maximum efficiency and stereospecificity of all enzymes: the resulting acetoacetyl-CoA incorporates **60% H** from water and **40% H** from **NADPH** (maximum possible from NADPH). Methylmalonyl-CoA epimerase (step 8) has a high likelihood of introducing water H at the α -C (“Step 8 water H”) (WÖLFLE et al., 1986), thus removing the H from the original acetyl CoA:

the resulting acetyl-CoA incorporates 2/3 (66.67%) H from water and 1/3 (33.33%) H from NADPH. If 4-hydroxybutyryl-CoA dehydratase (step 13) is highly reversible under physiological conditions, the 2 H at the ω -C also can be fully exchanged with H from water (Friedrich et al., 2008): the resulting acetyl-CoA (“Step 13 highly reversible”) would then incorporate 100% water-H and 0% from NADPH. We consider water introduction at step 8 highly likely, but preserve the original H at step 13, and thus base the modelling discussed in the main text on this scenario. Enzymatic steps are indicated with grey arrows. 1: Acetyl-CoA carboxylase, 2: Malonyl CoA reductase, 3: Malonic semialdehyde reductase, 4: 3-hydroxypropionyl-CoA synthetase, 5: 3-hydroxypropionyl-CoA dehydratase, 6: Acryloyl-CoA reductase, 7: Propionyl-CoA carboxylase, 8: Methylmalonyl CoA epimerase, 9: Methylmalonyl-CoA mutase, 10: Succinyl-CoA reductase, 11: Succinic semialdehyde reductase, 12: 4-Hydroxybutyryl-CoA synthetase, 13: 4-Hydroxybutyryl-CoA dehydratase, 14: Crotonyl-CoA hydratase, 15: 3-Hydroxybutyryl-CoA dehydrogenase, 16: Acetoacetyl-CoA β -ketothiolase. Most carboxylic acids are partly deprotonated at physiological pH but are shown fully protonated for simplicity.

Supplemental References:

- Friedrich P., Darley D. J., Golding B. T. and Buckel W, 2008. The Complete Stereochemistry of the Enzymatic Dehydration of 4-Hydroxybutyryl Coenzyme A to Crotonyl Coenzyme A. *Angewandte Chemie International Edition* 47, 3254–3257.
- Leavitt W. D., Flynn T. M., Suess M. K. and Bradley A. S., 2016. Transhydrogenase and Growth Substrate Influence Lipid Hydrogen Isotope Ratios in *Desulfovibrio alaskensis* G20. *Frontiers in Microbiology* 07.
- Wölfle K., Michenfelder M., König A., Hull W. E. and Rétey J., 1986. On the mechanism of action of methylmalonyl-CoA mutase: Change of the steric course on isotope substitution. *European Journal of Biochemistry* 156, 545–554.

Supplemental Table S1: Biphytane H Fractions (Number of H)

		H ₂ O					NADPH			GGR	H ₂ O Exch.
		f_{A-W}	f_{LS-W}	f_{GGR-W}	f_{RS-W}	f_{-W}	$f_{A-NADPH}$	$f_{LS-NADPH}$	f_{-NADPH}	f_{FAD}	f_x
No water exchange	BP0	39.44% (31.56)	0.83% (0.67)	10% (8)	0% (0)	50.28% (40.22)	19.72% (15.78)	20% (16)	39.72% (31.78)	10% (8)	0% (0)
	BP1	39.6% (30.89)	0.85% (0.67)	8.97% (7)	1.28% (1)	50.71% (39.56)	19.8% (15.44)	20.51% (16)	40.31% (31.44)	8.97% (7)	0% (0)
	BP2	39.77% (30.22)	0.88% (0.67)	7.89% (6)	2.63% (2)	51.17% (38.89)	19.88% (15.11)	21.05% (16)	40.94% (31.11)	7.89% (6)	0% (0)
	BP3	39.94% (29.56)	0.9% (0.67)	6.76% (5)	4.05% (3)	51.65% (38.22)	19.97% (14.78)	21.62% (16)	41.59% (30.78)	6.76% (5)	0% (0)
Max. water exchange	BP0	20% (16)	0% (0)	10% (8)	0% (0)	30% (24)	10% (8)	20% (16)	30% (24)	10% (8)	30% (24)
	BP1	19.66% (15.33)	0% (0)	8.97% (7)	1.28% (1)	29.91% (23.33)	9.83% (7.67)	20.51% (16)	30.34% (23.67)	8.97% (7)	30.77% (24)
	BP2	19.3% (14.67)	0% (0)	7.89% (6)	2.63% (2)	29.82% (22.67)	9.65% (7.33)	21.05% (16)	30.7% (23.33)	7.89% (6)	31.58% (24)
	BP3	18.92% (14)	0% (0)	6.76% (5)	4.05% (3)	29.73% (22)	9.46% (7)	21.62% (16)	31.08% (23)	6.76% (5)	32.43% (24)

Full accounting of H sources to the biphytanes of archaeal tetraethers for organisms producing acetyl-CoA autotrophically via the 3HP/4HB pathway (assuming water H:NADPH = 2:1, i.e., 0.6667:0.3333). See Eq. 6a and 6b for relevant equations. See also main text Figure 3 for visual scheme of biphytane biosynthesis, and main text Table 2 for summary of differences between BPs.

1 **Supplemental Table S2:** Potential NADP(H) Sources in *N. maritimus*. BLAST approach employed following (Leavitt et al., 2016).

<i>Enzyme name</i>	<i>NAD(P)H generating</i>	<i>Abbreviation</i>	<i>H-isotope category</i>	<i>Pathway</i>	<i>Nitrosopumilus maritimus SCM1 locus tag(s)</i>
Complex 1: NADH:ubiquinone oxidoreductase	Yes	Nuo	2b	N/A	N_mar_0276 to 0286
Ferredoxins	Yes	Fd	2b, 3	N/A	N_mar_0238, 0239, 1537, 1765
ferredoxin:NADP+ oxidoreductase	Yes	FNR	3	N/A	Nmar_0672
cytosolic NADP+-reducing hydrogenase	Yes	SH	3 or 2	N/A	Nmar_1389
cytosolic NADP+-reducing hydrogenase	Yes	SH	3 or 2	N/A	Nmar_0267
cytosolic NADP+-reducing hydrogenase	Yes	SH	3 or 2	N/A	Nmar_0253
NAD+ kinase	Yes	NADK	2	N/A	Nmar_0268, Nmar_0440, Nmar_0921
isocitrate dehydrogenase	Yes	IDH	2	TCA cycle	Nmar_1069, Nmar_1379
glucose-6-phosphate dehydrogenase	Yes	G6PDH	2	oxPPP, ED	Nmar_0168
6-phosphogluconate dehydrogenase	Yes	6PGDH	2	oxPPP	Nmar_0635
glucose dehydrogenase	Yes	GDHs	2	Modified EDs	Nmar_0369
non-phosphorylating glyceraldehyde 3-phosphate dehydrogenase	Yes	GAPN	2	EMP, ED, SP ED	Nmar_1608
NAD+-dependent glyceraldehyde phosphate dehydrogenase, phosphorylating	Yes	NAD+/GAPDH	2	EMP, ED, SP ED	Nmar_0831
D-glyceraldehyde dehydrogenase (NADP+)	Yes	NADP+/GADH	2	npED	Nmar_1608
2-ketoglutarate (oxoacid)/ ferredoxin oxidoreductase			2	TCA cycle	Nmar_0413, Nmar_0414
malate dehydrogenase	Yes		2	TCA cycle	Nmar_0338, Nmar_0676

2

3 /END